Journal of Coastal Research 000-000 Charlotte, North Carolina Month 2025

Development of an Optimized Survey Workflow for Sandy **Beaches with Mapping-Grade Mobile LIDAR**

Isabel A. Garcia-Williams^{†‡*}, Michael J. Starek^{‡§}, and Jacob Berryhill[‡]

[†]Department of Physical and **Environmental Sciences** Texas A&M University–Corpus Christi Corpus Christi, TX 78412, U.S.A. Corpus Christi, TX 78412, U.S.A.

‡Conrad Blucher Institute for Surveying and Science

§College of Engineering and Computer Science

Texas A&M University-Corpus Christi Corpus Christi, TX 78412, U.S.A.





ABSTRACT

Garcia-Williams, I.A.; Starek, M.J., and Berryhill, J., 0000. Development of an optimized survey workflow for sandy beaches with mapping-grade mobile LIDAR. Journal of Coastal Research, 00(00), 000-000. Charlotte (North Carolina),

Mapping-grade mobile LIDAR scanning (MLS) systems have increasing appeal for coastal surveying, because they are becoming more cost effective and compact in comparison to the more expensive, higher-caliber, survey-grade MLS systems. Despite the misconception that these systems are plug and play, they should be evaluated, and sources of error must be understood to generate consistent, accurate data. This study assesses a miniaturized, mapping-grade MLS system to develop an optimized, validated survey workflow for rapid coastal corridor mapping of sandy beaches. The MLS system, called the HiWay Mapper, integrates a Velodyne HDL-32E LIDAR scanner, a NovAtel inertial navigation system, and a FLIR Ladybug 360° spherical camera. A four-part framework is introduced, in which a series of rigorous experiments were conducted to evaluate and validate system performance to generate a repeatable workflow for collecting high-accuracy, three-dimensional point cloud data of sandy beaches and foredunes. The framework of (1) sensor characterization and setup, (2) quality assurance, (3) data processing and quality control, and (4) postprocessing will ultimately support the production of georeferenced digital elevation models (DEMs) to monitor geomorphology changes of sandy beach and foredune systems. The final workflow was evaluated on a 4-km stretch of sandy beach on Padre Island National Seashore, Texas. Two surveys were completed on 26 July 2022 and 22 September 2022 to provide examples of workflow repeatability and vertical root-mean-square error (RMSE) measures. The final DEM vertical RMSEs were 0.039 and 0.037 m, respectively. Cross-shore transects were also used to extract metrics to compute shoreline movement, beach width, dune slope, and beach slope to show seasonal dynamics. The experiments, results, and workflow presented herein, along with guidance, should benefit coastal researchers seeking to integrate mapping-grade MLS systems into their data collection workflow.

ADDITIONAL INDEX WORDS: Coastal remote sensing, coastal topography, digital elevation modeling, 3D point clouds, change detection.

INTRODUCTION

The use of mobile LIDAR scanning (MLS) systems in coastal environments has been increasing because of their precise, high-resolution data. They can collect detailed surface information of the beach and foredune while allowing flexible data collection and are fairly easy to operate (Bitenc et al., 2011; Nahon et al., 2019). Compared with small uncrewed aircraft system (UAS)-based photogrammetry or LIDAR for beach surveying, MLS systems are not as limited in high-wind conditions and don't need to abide by airspace regulations, provided the beach allows vehicular operation. MLS has the ability to collect dense, three-dimensional (3D) point clouds to derive digital elevation models (DEMs) at high spatial resolution. Data collection can be efficient and allows rapid sandy beach corridor mapping while enabling frequent repeat surveys. This, along with ease of deployment, makes MLS an ideal method of data collection for assessment of beach and lower foredune geomorphology (Lim et al.,

are usually advertised. Before they can be used for coastal surveys, their performance must be characterized and data collection workflows refined to ensure accurate, repeatable data are collected. It is also important that sources of error and sensor limitations are understood. MLS systems can be categorized into survey grade and

2013). However, these systems are not plug and play, as they

mapping grade. According to Olsen et al. (2013), the quality and ranging accuracy of the laser scanner and inertial measurement unit (IMU) determine whether an MLS system is survey grade (high quality) or mapping grade (lower quality). Lin et al. (2021) describes survey-grade systems as having millimeter to centimeter accuracy and mapping-grade systems as having centimeter accuracy. This is validated by Olsen et al. (2013), who concluded that a mapping-grade MLS system can achieve vertical accuracy of approximately 2.5 to 6.5 cm, depending on the range to the target and system capabilities, among other factors.

Consequentially, the difference between survey and mapping grade depends not only on quality but also on the cost of the system and often the system form factor (i.e., size) for achieving that quality. A survey-grade MLS system is equipped with higher-quality components and can cost several hundred thousand U.S. dollars. In contrast, mapping-grade

DOI: 10.2112/JCOASTRES-D-24-00056.1 received 19 July 2024; accepted in revision 26 November 2024; corrected proofs received 24 May 2025; published pre-print online 20 June 2025.

^{*}Corresponding author: igarcia21@islander.tamucc.edu

[©]Coastal Education and Research Foundation, Inc. 2025

systems can be up to 10 times cheaper (Elhashash, Albanwan, and Qin, 2022). According to Hauser, Glennie, and Brooks (2016), survey-grade systems can be large, difficult to operate, and demanding of both resources and time. In contrast, most mapping-grade MLS systems are specifically designed to be compact. This allows the system to be rapidly and more easily deployed (Brooks *et al.*, 2013).

It is evident that mapping-grade systems don't achieve the same level of precision as survey-grade systems. This was demonstrated in a study conducted by Lin et al. (2021) who compared the performance of mapping- and survey-grade MLS systems to that of a terrestrial laser scanning (TLS) system for bridge monitoring. They found that after undergoing a rigorous registration process, the point cloud quality was 1.5 cm for mapping-grade MLS, 0.7 cm for survey-grade MLS, and 0.6 cm for TLS. Mapping-grade MLS systems still provide acceptable accuracy that aligns with standards for a range of applications. They are a cost-effective, lightweight, and reliable choice for fields such as earth sciences and lower-accuracy engineering projects (Hauser, Glennie, and Brooks, 2016). With these considerations, mapping-grade MLS was applied in this study, because it delivers sufficient vertical accuracy for sandy beach corridor mapping, making it an optimal tool for repeat surveying of beaches for supporting quantitative coastal analyses, such as monitoring beach elevation change and morphology.

MLS systems, in general, can be deployed on different types of static and moving platforms including on the ground, such as on a vehicle or backpack scanner, in the air such as on an airplane or UAS, and on water-based vessels. MLS in the context of this paper refers to MLS systems deployed on vehicles operating on the ground. This mode of operation allows for the continuous collection of dense, georeferenced 3D point cloud data over a fairly large spatial scale at relatively high vehicle speeds (Johnson et al., 2016; Wang et al., 2018). Some MLS systems can achieve high vertical accuracy, resulting in precise DEMs with high spatial resolution. In addition, some mapping-grade systems have the ability to achieve survey-grade accuracies in certain scenarios. The ease of mobility of MLS systems deployed on moving vehicles also allows quick deployment for poststorm data collection in high-wind conditions (Gong, 2013; Lim et al., 2013).

MLS systems have certain limitations, including varying point density caused by radial scanning and decreasing geometric accuracy as objects move farther distances away from the sensor (Holopainen *et al.*, 2013). There is also limited access because driving space is needed, and the beach of interest needs to be accessible by vehicle. This is unfavorable for high tides or difficult terrain, where it would be easier to fly an airborne laser scanner (ALS; Lim *et al.*, 2013). MLS also cannot map occluded features such as terrain behind the foredunes and the tops of dunes because of the oblique perspective of the sensor (Bitenc *et al.*, 2011; Nahon *et al.*, 2019; Wang *et al.*, 2018).

Sources of error in MLS systems can be attributed to many factors, the largest of which include global navigation satellite system (GNSS) and inertial navigation system (INS) position and orientation errors, IMU misalignment, sensor boresight calibration, and lever arm offsets. Another source stems from

the LIDAR sensor, which can result in ranging errors, beam divergence, and laser calibration errors (Hurst, 2014). GNSS positioning errors can be influenced by multipath errors, position dilution of precision (PDOP), clock error, and base station errors used for differential trajectory correction. Other contributing factors are random noise, systematic errors such as improper datums, and human-induced factors (CALTRANS, 2018; Lim *et al.*, 2013; Olsen *et al.*, 2013).

Although MLS systems are becoming more widely used for coastal zone monitoring, literature is still scarce for applications on sandy beaches (Gong, 2013). Previous research successfully deploys MLS for topographic surveying, poststorm damage, and change detection at varied accuracies. Bitenc et al. (2011) surveyed 6 km of a flat, dune-flanked sandy beach in the Netherlands at low tide to analyze the quality of MLS-derived point clouds and DEMs. Quality control (QC) was completed using a point-to-point comparison between overlapping point clouds, and the DEM was computed using linear interpolation. Results found that MLS systems can achieve a root-mean-square error (RMSE) of 0.050 m with a product available within 2 days of data acquisition. Vaaja et al. (2011) used MLS to observe accretion and erosion in northern Finland. Data were collected twice over the course of 2 years and compared using DEMs. The resulting RMSE values of the LIDAR-derived DEMs were between 0.023 and 0.076 m. Barber and Mills (2007) surveyed a 7-km stretch of flat, sandy beach abutted by soft cliffs in North Yorkshire, United Kingdom. The vehicle was driven at a maximum speed of 32 km/h, which took approximately 15 minutes to complete one pass. The resulting processed dataset was 550 MB and included more than 20 million points. The accuracy of the MLS system and its derived DEM was then assessed and compared with that of an ALS and surveyed checkpoints over two test sites within the study area. RMSEs of the datasets, compared with the checkpoints, were 0.222 and 0.200 m for both sites. Lastly, Lim et al. (2013) mounted a TLS on a vehicle to assess horizontal and vertical accuracy when used in coastal mapping on both a sandy beach and a paved road on Padre Island National Seashore (PAIS). The conducted survey was 12 km long; 12 ground control points (GCPs) were surveyed for use as checkpoints, but only 6 GCPs were identifiable. Before adjustments, the mean errors were 0.222 m (X). 0.036 m (Y), and 0.104 m (Z). From the survey, boresight and lever arm adjustments were made and the point cloud mean errors were computed, equaling 0.060 m (X), 0.095 m (Y), and 0.053 m (Z).

Although these studies investigated the accuracy of MLS systems for use in coastal settings, none created a complete survey workflow specifically tested and evaluated for rapid corridor mapping of sandy beaches. Olsen *et al.* (2013), Johnson *et al.* (2016), the California Department of Transportation (CALTRANS, 2018), and others have created workflows for using MLS in urban applications. These were used as references for this project, but some recommendations do not apply to the dynamics of coastal environments. In addition, parts of these workflows do not report justification of the resulting recommendations or testing results (Johnson *et al.*, 2016).

With continued technological advancement and development of lower-cost, compact MLS systems, leading to more cost-effective options and wider use, their appeal to coastal zone monitoring will likely grow. However, as previously explained, mapping-grade MLS systems generally are not expected to perform at the level of accuracy and precision of higher-end survey-grade MLS systems. These systems often require additional testing and evaluation to improve data fidelity. The goal of this research is to develop an optimized survey workflow for generating repeatable, accurate, rapid 3D point cloud data for generating DEMs of sandy beach corridors with a mapping-grade MLS system. The workflow presented herein encompasses the evaluations required to ensure that an MLS system is capable of systematically collecting consistent and reliable data for sandy beach surveys. The methods, results, and case study are presented in the following four phases: (1) sensor characterization and setup, (2) quality assurance, (3) data processing and QC, and (4) postprocessing.

Study Areas

Four study sites were chosen for various tests and procedures, as pictured in Figure 1. The first was downtown Corpus Christi, selected for its large buildings to complete sensor characterization and setup. Second, the Texas A&M University—Corpus Christi (TAMU-CC) Ward Island campus was used to assess some sensor characterization and setup, quality assurance, and postprocessing procedures. Third, a section of sandy beach on North Padre Island, Texas, was the study site for evaluating the experiments' quality assurance, data processing, and QC. Lastly, a section of sandy beach on Malaquite beach, a pedestrian-only beach located on PAIS, was the case study site, used to demonstrate the effectiveness of the final workflow.

Equipment

The mapping-grade MLS system used in this study is called the HiWay mapper, as pictured in Figure 2, was integrated by LiDARUSA (Hartsell, Alabama, U.S.A.), and includes a Snoopy A series and a FLIR Ladybug5+ (Wilsonville, Oregon, U.S.A.). The Snoopy A series is also an integrated system and is comprised of a Velodyne HDL-32E LIDAR (San Jose, California, U.S.A.) and a NovAtel Position and Orientation System (POS) (Calgary, Alberta, Canada). The Velodyne has a spinning head which contains 32 class 1, near-infrared (NIR) 903-nm laser pairs and a receiving window. It collects approximately 700,000 points per second (pts/s) in single return mode and approximately 1,390,000 pts/s in dual return mode (Velodyne Lidar, Inc., 2018), with a user-defined spinning rate of 5 to 20 Hz (Alsadik, 2024), set at 20 Hz for this study. This LIDAR has an effective range of up to 100 m in single return mode with ± 2 -cm accuracy (one sigma at 25 m; Hurst, 2014).

The GNSS is a NovAtel 702gg that measures both GPS and Globalnaya Navigationnaya Sputnikovaya Sistema (GLONASS), reads L1 and L2 wavelengths, and contains a single antenna. The INS is a NovAtel SPAN-IGM, featuring a Sensonor STIM300 IMU (Vestfold, Norway) and a NovAtel OEM615 receiver. It has three microelectromechanical system (MEMS)—based gyroscopes, three accelerometers, and three stability

inclinometers and collects at 125 Hz (Safran Sensing Technologies, 2019). The GNSS and INS together form the position and orientation system (POS).

The HiWay mapper was also integrated with a FLIR Ladybug5+ 360° spherical camera, as pictured in Figure 2. The resolution is 2448 by 2048 pixels, has a field of view (FOV) of 90% of a full sphere, and is accurate to 2 mm at a 10-m distance. It collects up to 30 frames per second, has 30 megapixels (5 megapixels \times 6 sensors), and a pixel size of 3.45 μm (Teledyne FLIR, 2023).

WORKFLOW FRAMEWORK AND ESSENTIAL COMPONENTS

This section summarizes the key steps used to develop a workflow for using mapping-grade MLS systems in sandy beach environments. These key components are outlined in Figure 3 and are addressed in four phases. This section provides background research to address why key workflow components are needed and what actions are required to complete these steps. For certain key steps, multiple approaches are presented to accommodate varying access to software and tools. The purpose is to prepare a systematic, adaptable workflow that can be applied, or partially applied, to any mapping-grade system used on a sandy beach corridor, regardless of the user's experience level. All components are critical for optimizing a mapping-grade MLS workflow to achieve the best-quality data with a lower-cost system. The workflow elements are compiled to minimize the error budget, reduce costs, accelerate data delivery, and increase data fidelity. It is written and organized as a workflow.

Sensor Characterization and Setup

Sensor characterization and setup of the MLS system is an essential step to ensure that a user is ready to begin collecting 3D point cloud data in a coastal environment. The mounting platform must be stable, correct lever arm and LIDAR and camera boresight values must be used, and the effective range of the LIDAR must be known to produce precise and accurate point clouds.

System Mounting and Stabilization

A rigid platform is essential for mounting and securing the LIDAR, IMU, camera, GNSS antennae, and other elements. An example of a rigid frame is pictured in Figure 2, where the MLS is mounted on a metal plate on the roof of a utility task vehicle (UTV; Figure 2a) and on suction cups on the roof of a 4WD truck (Figure 2b). The mount may come from the system provider, or a custom setup can be built according to a user's needs.

Lever Arm Measurement

Lever arm offsets are the GNSS receiver's positional offsets in relation to the IMU body frame origin. Additionally, lever arm offsets are also the LIDAR system's positional offsets in relation to the IMU body frame origin. They directly contribute to the production of accurately georeferenced and aligned data. Use of incorrect lever arm values can cause inconsistencies in multiple passes, resulting in object doubling and misalignment. For static rigid mounts, lever arm offsets should only need to be measured once unless displacement occurs on the mount, in the sensor, or in another component. They can

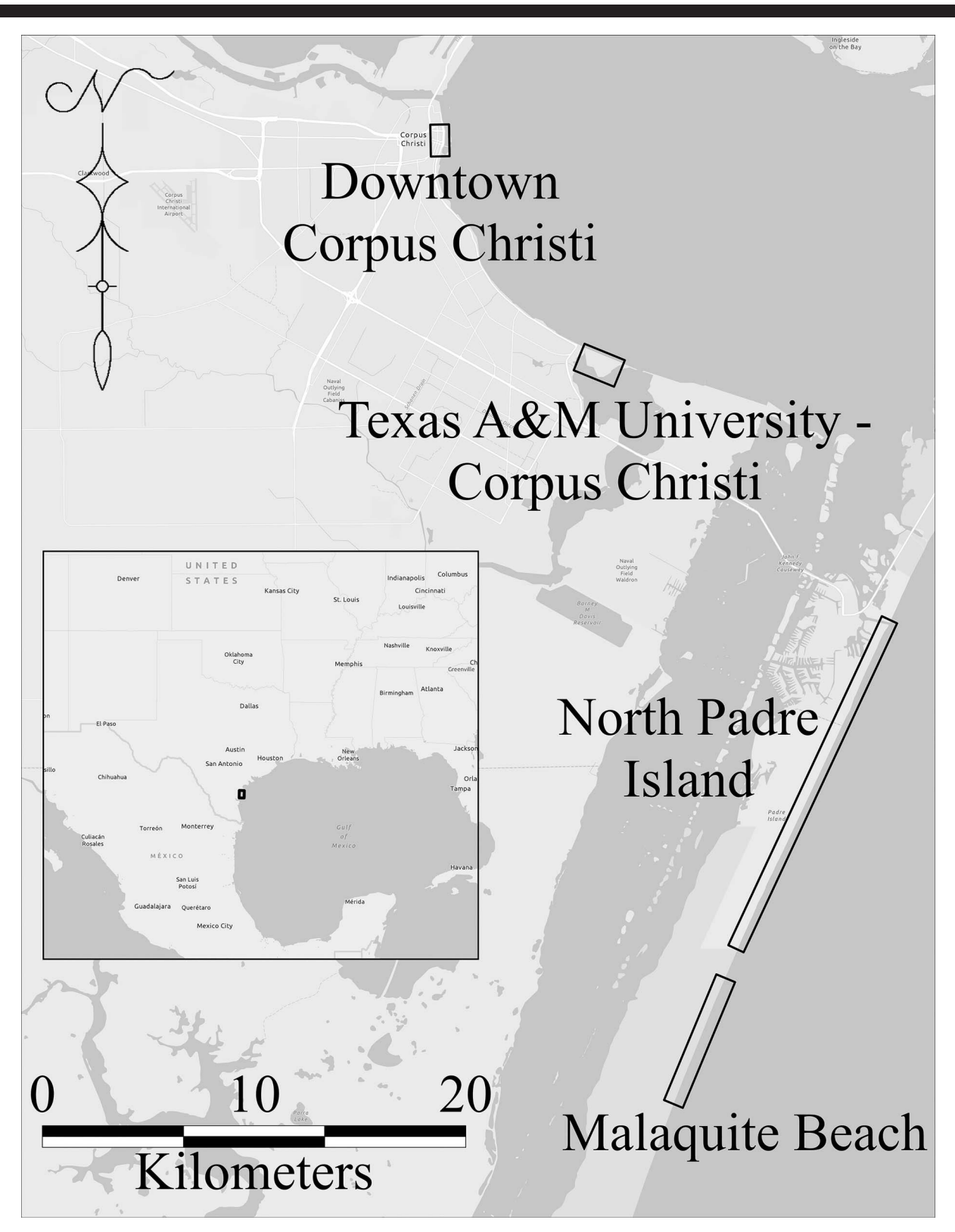


Figure 1. Locations of the study sites around Corpus Christi, Texas.



Figure 2. HiWay Mapper mapping-grade MLS system mounted on (a) a custom metal plate fitted over the roof of a UTV and (b) suction cups on the roof of a 4WD vehicle.

be physically measured and later adjusted through boresight calibration procedures (Guan *et al.*, 2016; Johnson *et al.*, 2016; Olsen *et al.*, 2013). According to Olsen *et al.* (2013), lever arm offsets can only be measured to an accuracy of 0.5 cm in the X, Y, and Z axes because of the assumptions made when measuring these components. An example of this is the assumption that the IMU is located exactly where the system drawings depict it, and the IMU and LIDAR axes are aligned.

LIDAR Boresight Calibration Validation

LIDAR boresight calibration solves the angular orientation of the LIDAR sensor frame with respect to the IMU body

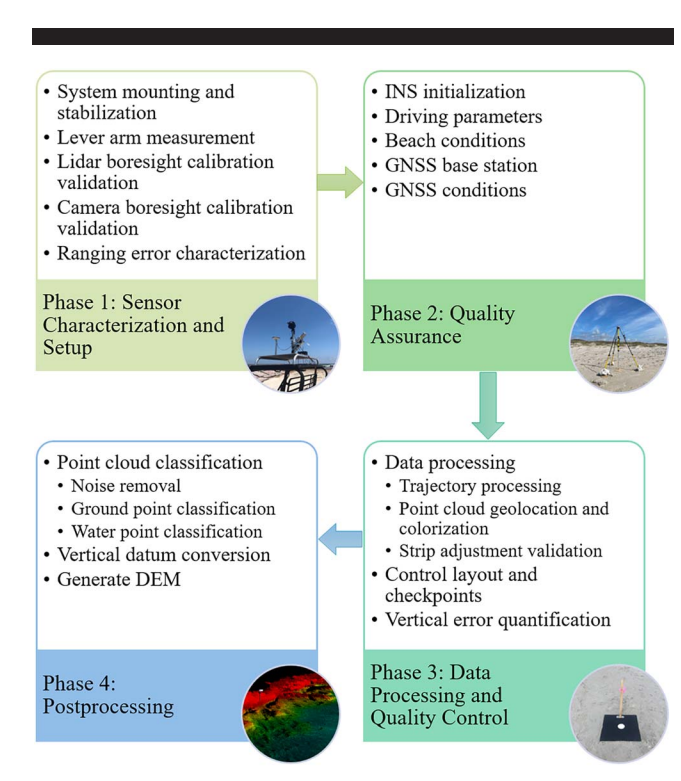


Figure 3. Four phases of the mapping-grade MLS system survey work-flow presented in this study and key components.

frame origin. Incorrect values can result in positional errors in the postprocessed MLS point cloud data, such as object doubling, shifts in data, and misalignment between multiple passes. These result from alignment errors in the heading roll and pitch between the lidar sensor and INS, which propagate over a distance (Guan et al., 2016; Johnson et al., 2016; Olsen et al., 2013). As with lever arm measurements, these should be calculated once and occasionally validated as part of routine system assessment. This is especially true if conditions change or the system has experienced prolonged use, potential flexure, or other impacts. Minor adjustments to these values can be calculated using strip adjustment, which is discussed later in this paper, while the implementation of a lidar boresight calibration can also provide minor adjustments to the lever arm measurements.

Camera Boresight Calibration Validation

Camera boresight calibration solves the orientation of the camera with respect to the IMU body frame origin. Camera boresight calibration errors cause misalignment between the georegistered imagery and the LIDAR point clouds, resulting in falsely colorized points. These values should be provided by the manufacturer but also should be validated upon receipt of the system and updated as part of routine care. Furthermore, camera boresight values can be refined during post-processing when registering the imagery to a point cloud. This adjustment process enhances the quality of the dataset by correcting slight misalignments and improves the overall calibration of the system.

Ranging Error Characterization

Determining an optimal effective scanning range for an MLS system is essential for both planning a survey and post-processing. A LIDAR sensor ranging error can decrease the resulting point cloud's accuracy and fidelity. The range reported by a system manufacturer is often the maximum range, tested under laboratory conditions with highly reflective targets (Aevex Aerospace, 2024). According to Baraja (2021) and Huntington and Williams (2024), a LIDAR's range depends on a combination of the following: sensitivity of the receiver, strength of the return pulse, beam divergence, target reflectivity, target angle, and atmospheric effects. LIDAR systems typically have a minimum return strength detection

threshold, thus filtering out noise and limiting false and unwanted returns. There are also many factors that can affect the beam as it travels to a target and as the return pulse travels back to the sensor. One of these is beam divergence, which is the spread of the pulse over a distance. Typically, a LIDAR's beam divergence can be found on the datasheet (measured in milliradians). In addition, target reflectivity and incident angle of the outgoing pulse can affect the return pulse. For example, dune vegetation can contain leaves and thin stems that can result in partial and deflected returns. Furthermore, damp sand can partially absorb a NIR pulse, resulting in weaker returns, whereas dry sand will have a higher return value. The atmosphere also affects the effective range of a LIDAR. Although these systems should not be used in dense fog, rain, and other poor conditions, sea spray is inevitable when surveying sandy beaches. These conditions cause beam absorption and scattering, which affect the outbound and return beams (Baraja, 2021; Huntington and Williams, 2024).

Quality Assurance

A structured methodology for survey design and quality assurance is essential for survey repeatability and maximizing the resulting point cloud accuracy. Before conducting a survey, proper reconnaissance must take place to (1) plan the order of events, (2) ensure apt setup and initialization, (3) plan driving parameters, and (4) ensure appropriate GNSS coverage and baseline length. This section describes the steps to ensure each survey is systematically planned and managed and the best-quality data are collected.

INS Initialization

Initializing an INS before data collection is often essential to provide the IMU an initial position, velocity, and attitude. Doing so can decrease GNSS latency errors which can be incorrectly attributed to sensor noise due to IMU misalignment (NovAtel, 2013). However, the specific initialization procedure required will depend on the INS used. Therefore, it is crucial to consult the system documentation to determine the recommended procedures.

As an example, the INS used in this study is a MEMS-IMU. According to the system's documentation, initial position, velocity, and attitude are zero. The GNSS receiver then begins receiving satellite signals, prompting a coarse time estimate. When more satellites are available, an initial position is solved and is accurate enough to start timing IMU measurements. After, an IMU bias is computed, which prompts the start of either a coarse alignment or a kinematic alignment. A coarse alignment measures Earth's rotation and gravity using the accelerometer and gyroscope measurements to compute the initial roll, pitch, and heading, a process which takes about 45 seconds. According to Yang et al. (2022), The gyroscopes in MEMS-IMUs often struggle to calculate initial heading accurately during a coarse alignment, so it is important to begin INS alignment in the direction that collection will take place. A kinematic alignment uses the GNSS velocity vector to calculate the INS systems heading. It is also recommended by the manufacturer that any driving procedures should keep the vehicle roll to less than

10° during this process to keep it parallel to the frame of the vehicle (NovAtel, 2013).

This example highlights the specific considerations for the system used in this study. Each INS has unique requirements and operational procedures that must be carefully followed to ensure accurate data collection. Failing to adapt to these requirements may compromise the integrity of the collected data and introduce errors that this step is trying to eliminate through proper initialization and alignment.

Driving Parameters

Driving parameters should be considered when planning and conducting an MLS survey. These can include driving speed, local laws, sand conditions, and scan line overlap and spacing. Driving speed depends on local laws, desired point density, and beach conditions. Bech driving regulations and conditions differ depending on the location. In addition, surveys conducted on restricted beaches may require permits and may need to adhere to special restrictions.

The number of scan lines, along with scan overlap and spacing, is determined by beach width, beach terrain, the effective range of the laser scanner, and targeted sidelap. If the MLS system is mounted on the roof of a vehicle with a bed, the resulting point cloud will likely contain occlusion, and an extra pass or passes will ensure full coverage of the beach. According to CALTRANS (2018), a minimum of 25% sidelap should be implemented. Recommendations for sidelap in ground-based MLS surveys are not extensively documented in literature. As such, it is recommended to consult the manufacturer's documentation and perform site-specific tests to determine appropriate sidelap requirements based on the survey environment, system specifications, and data quality objectives. In this study, the system manufacturer, LiDARUSA, recommended 30 to 50% sidelap. The effective range (as determined by the sensor ranging error characterization) plays a key role for determining the number of scan lines needed to survey sandy beaches, because it establishes the distance between scan lines. The distance between scan lines (D_{SL}) can be computed using the following equation:

$$D_{SL} = R_{lidar} + Sidelap \tag{1}$$

where, R_{lidar} is the effective range of the LIDAR scanner and $Sidelap = \%Overlap * R_{lidar}$. This concept is visualized in Figure 4. The number of scan lines (N_{SL}) for a beach of X width can then be found with:

$$N_{SL} = \left[\frac{Width - 2R_{lidar}}{D_{SL}}\right] + 2 \tag{2}$$

where Width is the width of the respective beach to be surveyed.

Beach Conditions

Metocean conditions such as wave runup, tidal conditions, wind, and currents affect the amount of exposed beach and should be considered when planning the number of scan lines needed and the survey date (Pennington *et al.*, 2024). Wind, waves, and weather conditions can be found on various weather sites and apps and can provide future predicted conditions. Some important weather elements to consider are

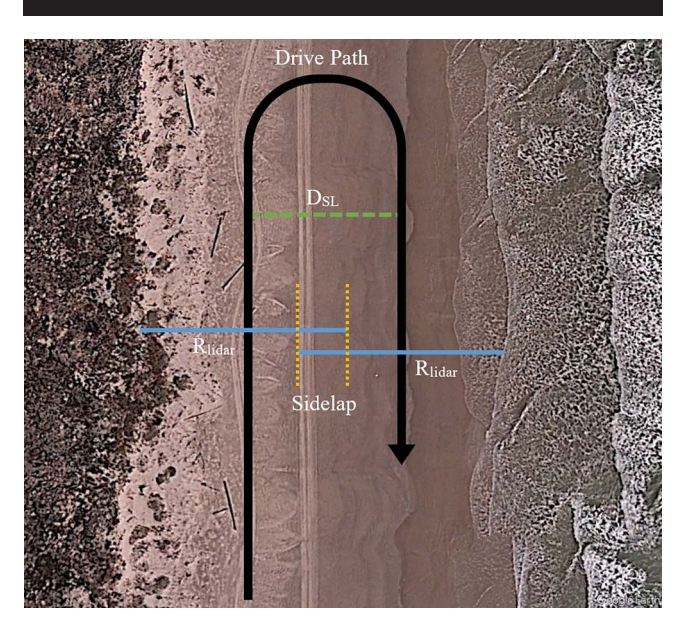


Figure 4. Illustration of the distance between scan lines (D_{SL}) considering lidar range (R_{lidar}) and targeted sidelap.

wind speed, gusts, and direction; wave direction and height; cloud cover; and temperature. It is preferrable to target offshore winds and low tide to expose the beach, berm, and foreshore to capture mean high water (MHW) or another tidal datum (White, 2007). In the United States, tide predictions at certain gauge stations can be viewed using National Oceanic and Atmospheric Administration's (NOAA's) tide and current predictions (NOAA, 2024b). Inundation predictions can be viewed on NOAA's inundation dashboard (NOAA, 2024a).

GNSS Base Station

A GNSS base station is a requirement for performing postprocessed kinematic (PPK) correction of the MLS system's GNSS trajectory (CALTRANS, 2018). It can be categorized as local and public. A local base station is an independent reference station that is established and operated for a minimum of the duration of the corresponding MLS survey. It can also be used to run a real-time kinematic (RTK) network to establish control along the project site when public networks are not available. According to Johnson et al. (2016) and CALTRANS (2018), a base station should be located central to the project area and collect at 1 Hz or better. Baselines should be kept relatively short to achieve higher-quality data: no more than 16 km in length, although up to 14.5 km is ideal (CALTRANS, 2018; Olsen et al., 2013). For larger projects, Johnson et al. (2016) recommends multiple base stations. If a local base cannot be established, a nearby and publicly available continuously operating reference station (CORS) can be used, as there is a dense network throughout the United States.

GNSS Conditions

It is important to target favorable satellite position and orientation of constellations recorded by all GNSS receivers.

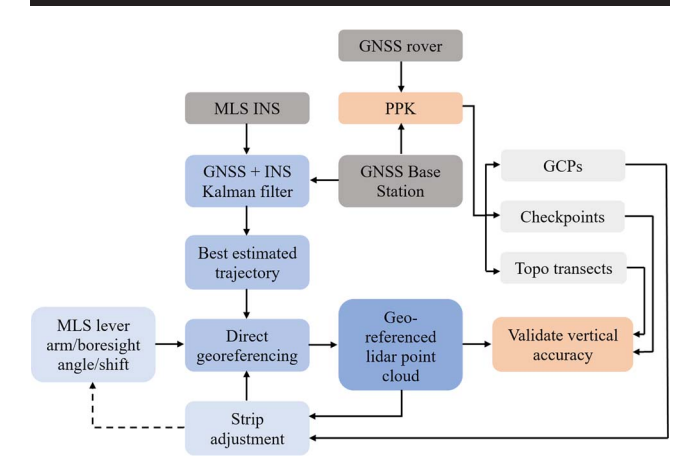


Figure 5. Data processing and QC workflow.

The survey site should be properly reviewed to ensure that there will be few to no obstructions (i.e. tall hotels, power lines, cliff structures), particularly for selecting a base station location and driving paths (Olsen et al., 2013). This can be done by checking the PDOP and sky plots of satellite locations for a given coordinate and time frame. Because PPK corrections are used to adjust the MLS system trajectory, these measurements define the overall georeferencing accuracy of the resulting point cloud. The GNSS receiver's user manual usually states the satellite constellations that it registers. Websites are available to plan surveys on a day with favorable satellite position and orientation, such as Trimble GNSS Planning (Trimble, 2024) and GNSS Mission Planning (Navmatix, 2024). A GNSS cutoff angle is also important to consider to mask satellite signals closer to the horizon to reduce atmospheric refraction. A base cutoff angle of 10° to 15° is recommended by NGS (2014).

Data Processing and Quality Control

This section describes the processes used to generate, adjust, and validate an MLS system survey. Through a series of operations and QC measures, an accurate and reliable point cloud can be produced. Data processing includes trajectory processing, point cloud geolocation, and strip adjustment. Afterward, QC takes place to adjust the point cloud. The processes that take place in this phase are outlined in Figure 5.

Data Processing

Data processing takes place using the following steps: (1) the trajectory is processed, (2) a point cloud is created and colorized (if imagery was collected), and (3) strip adjustment takes place, during which GCPs can be applied.

Trajectory Processing. Trajectory processing computes the LIDAR's position and attitude at any given point in time. It is created by processing the MLS system's GNSS rover and INS data simultaneously, using a loosely coupled, a tightly coupled, or an alternate method. In a loosely coupled architecture, the GNSS positions and INS solutions are viewed as two independent variables. The GNSS-estimated position,

velocity, and times are usually used to update the INS solution through a Kalman filter (Falco, Pini, and Marucco, 2017). The errors of this solution are then resubmitted to INS processing to correct IMU errors and thus further improve the final solution. A tightly coupled method processes the GNSS raw measurements, such as pseudorange and Doppler shift, and the INS solutions through a centralized Kalman filter (Falco, Pini, and Marucco, 2017) to generate the best estimated trajectory. In most cases, tightly coupled architecture may provide a better solution, as seen in Falco, Pini, and Marucco (2017). This is particularly true in areas where there is poor GNSS coverage or during surveys with long, straight stretches during which a lack of dynamic driving can cause IMU drift (Chen, Wang, and Yang, 2023; Falco, Pini, and Marucco, 2017). In addition, a trajectory can be processed in a forward direction, reverse direction, or both. In forward processing, the data are processed in the order that they were collected. In reverse processing, data are processed from the end of the survey to the beginning. According to NovAtel (2024b), combining the solutions maximizes accuracy and acts as a type of QC.

Point Cloud Geolocation and Colorization. Point cloud geolocation and colorization use the processed trajectory and the following components to create and colorize a point cloud. The INS measures the position and orientation of the sensor head for each emitted laser pulse's range and scan angle through a process called direct georeferencing. The LIDAR boresight angles, lever arm offsets, and processed trajectory are also used. These enable the LIDAR scanner measurements (notably, range and scan angle) to be converted into a geographically referenced set of X, Y, and Z coordinate measurements (i.e. a georeferenced point cloud) relative to a geodetic datum and projected coordinate system. The Z values are initially referenced to ellipsoid heights but can be converted into an orthometric vertical elevation using an appropriate geoid model (Olsen et al., 2013). The LIDAR scanner's effective range should be defined by applying a maximum distance filter to ensure that no data points are generated beyond that range. Minimum range varies by vehicle and sensor setup to eliminate unwanted points from the back of the vehicle or sensor frame. Point cloud colorization may take place after a point cloud is processed if imagery was collected. It should be noted that this will ideally take place after a strip adjustment is performed, but that may be dependent on the tools used. In this workflow it is performed and thus placed before strip adjustment. In the process, camera boresight values and the GPS time each image was captured are used to register the imagery to the point clouds. The colorization process can be validated by using ground-truth data and observing alignment with nonground objects such as vehicles, signposts, and power lines.

Strip Adjustment Validation. Strip adjustment validation verifies the impact of a strip adjustment. This process registers two or more adjacent scan lines together, ensuring they are accurately aligned to one another. Offsets in overlapping scan lines cause object misalignment and reduce the overall accuracy of the point cloud (Chen, Li, and Yang, 2021). This can be caused by trajectory errors, such as incorrect boresight

and/or lever arm values, or POS drift during data collection (Kuçak, Erol, and Erol, 2022). Strip adjustments use algorithms to adjust two or more scan lines by locating common tie lines or points in each and solving for errors in easting, northing, elevation, roll, pitch, and heading. They also can provide minor boresight and lever arm corrections that can be used to update the current values (Avevex Aerospace, 2024; Lewis, 2021).

Control Layout and Checkpoints

Georeferencing errors may occur during a survey because of INS drift, poor GNSS coverage, and other influences. To address these issues, control points are essential for adjusting the point clouds effectively. CALTRANS (2018) recommends GCP spacing of no more than 152 m for type A surveys (hard-surface topographic surveys) and no more than 457 m for type B surveys (environmental and low-accuracy topographic surveys). Abdulrahman et al. (2013) recommends a minimum of 3 GCPs per site, with 20 GCPs or more being optimal for their study site of 91,000 km². These recommendations are based on urban areas where GCP placement is limited (Guan et al., 2016; Olsen et al., 2013). In coastal corridor mapping, there is more flexibility for target placement and an opportunity to lay targets in the center of the beach if that yields more accurate results and if waves, tides, etc. allow it.

Along with GCPs, QC checkpoints are vital to quantify errors (Kalvoda, Nosek, and Kalvodova, 2021; Olsen et al., 2013). These points must be broadly distributed throughout the site to reflect variance of the project terrain (Johnson et al., 2016; Olsen et al., 2013). CALTRANS (2018) recommends a minimum of five checkpoints per 1.6 km. Olsen et al. (2013) recommends checkpoints spaced 150 to 300 m for accuracy level 1 (minimum point density of 100 pts/m² and 3D network accuracy of 5 cm at 95% confidence), 300 to 750 m apart for accuracy level 2 (minimum point density of 30 pts/m² and 3D network accuracy of 20 cm at 95% confidence), and 170 to 1500 m for accuracy level 3 (minimum point density of 10 pts/m² and 3D network accuracy of 1 m at 95% confidence). Lastly, the American Society of Photogrammetry and Remote Sensing's (ASPRS) Positional Accuracy Standards, edition 2 (ASPRS, 2024) recommend a minimum of 30 checkpoints to validate MLS surveys.

Vertical Error Quantification

Vertical error is typically computed using RMSE, which is defined by:

$$RMSE_{z} = \sqrt{\frac{\sum_{i=1}^{n} \left(Z_{data(i)} - Z_{check(i)}\right)^{2}}{n}}$$
(3)

where, Z_{data} is the Z coordinate of the point cloud or DEM product and Z_{check} is the Z coordinate of the corresponding checkpoint (ASPRS, 2004). This should typically be computed to evaluate the vertical accuracy of the point cloud, which is a function of the horizontal accuracy and the beach slope. After the point cloud is filtered and a DEM generated, it should be computed again. It can usually be calculated in point cloud processing software and is normally computed after applying GCPs. Two forms of accuracy assessment can be used: targeted checkpoints and topographic checkpoints. Targeted

checkpoints can supplement the use of GCPs, provide a second form of point cloud validation, and be used to compute horizontal accuracy. Collecting cross-shore topographic transects of the beach, from the shoreline to the dune toe, provides more ground cover over a wider variety of landscapes. This is essential near the dunes and shoreline where targeted checkpoints are not usually placed. Vegetated vertical accuracy is computed from topographic checkpoints collected in areas with weeds and other plants, such as those above the vegetation line on a foredune (ASPRS, 2024).

Postprocessing

Data postprocessing procedures filter the georeferenced point cloud and produce a bare-earth DEM. The quality and accuracy of the DEM depends largely on how well a point cloud is classified and interpolated. Various software and tools can be used during this phase of the workflow, but this discussion focuses solely on the main steps implemented to produce a high-quality DEM of the beach surface from the output point cloud data.

Point Cloud Classification

Classifying a point cloud removes noise, and classifies ground points, water, and other unwanted points to facilitate seamless generation of a bare-earth DEM.

Noise Removal. Noise removal isolates unwanted points while preserving wanted features (Rakotosaona $et\ al.$, 2020). Common point cloud software have noise classification tools; for example, LAStools' lasnoise module can remove noise using a gridded filter with 3D cells of x by x by x size, which are assigned to a point, with the point in the center. Based on user-based criteria, isolated points are then removed. In addition, Terrasolid classifies isolated groups of a user-specified number as noise. Deep learning and artificial intelligence approaches can also be used. An example is the method described in Rakotosaona $et\ al.$ (2020) which uses deep learning to find and remove noise.

Ground Point Classification. Ground point classification removes nonground points such as vegetation, vehicles, mile markers, and bollards. They can be completed using several methods. One common filter, the progressive morphological filter, classifies ground and nonground features to allow the removal of nonground points. This method uses an iterative filtering window of size x, which gradually grows with each progression. It dilates or erodes features and uses neighborhood points to classify ground (Zhang et al., 2003). LAStools' lasground is based on Nie et al. (2017), which uses a revised progressive triangulated irregular network (TIN) densification algorithm, which accepts a series of input parameters, such as maximum slope, terrain type, and window size. It then finds the lowest point in each cell and iterates to judge and classify all points in the cell as ground or nonground. Bailey et al. (2022) compared three classification methodologies. First was an inverted cloth simulation filter (CSF), which acts as a cloth draped over an upside-down point cloud that uses a threshold for slope, resolution, etc., to classify. Second was a modified slope-based filter, which mainly uses slope and height between neighboring cells to determine ground points. Third was a random forest supervised machine learning algorithm that uses decision trees to determine whether points are ground or nonground. The study concluded that overall, CSF performed the best when the parameters were chosen carefully. Qin et al. (2023b) evaluated different methods of supervised deep learning to classify various terrains. They found that the classified dataset, called OpenGF, could be used to train other advanced deep learning models and is an effective and efficient method of classifying ground points. Lastly, Qin et al. (2023a) provided a comprehensive review of both supervised and unsupervised ground filtering methods.

Water Point Classification. Water point classification removes unwanted noise caused by water, such as returns scattering from breaking waves, seafoam, wave runup, and other ocean surfaces in the intertidal zone. Because water absorbs, or partially absorbs, NIR pulses, it is common for water and wet sand to have a low reflectance value when using an MLS with an NIR laser pulse. Brzank and Heipke (2012) used LIDARderived parameters and fuzzy logic to classify water and ground with more than 90% accuracy. The accuracy was lower in areas of wet sand, because the elevation, location, and intensity were closely related to those of water. Smeeckaert et al. (2013) used a supervised support vector machine classification, which used height, local point density, and 3D point distribution to obtain more than 90% accuracy. An elevation contour may also be used as a proxy to remove water. Furthermore, colorized point clouds can be used for classification or manual delineation, because red-green-blue (RGB) parameters can be used, in addition to intensity.

Vertical Datum Conversion

MLS system trajectory data in the vertical component are typically referenced as ellipsoid heights in the same geodetic datum as the local GNSS base station used to correct the MLS trajectory. If the generated point cloud data are also referenced in ellipsoid heights, then they typically must be converted to an orthometric vertical datum using an appropriate geoid model for DEM creation. In the United States, it is common to convert ellipsoid heights referenced to the North American Datum of 1983 (NAD83) to North American Vertical Datum of 1988 (NAVD88) using a National Geodetic Survey (NGS) geoid model, such as GEOID18 (NGS, 2020). It is commonplace for point cloud processing software to have the capability to export trajectory data in either ellipsoid or orthometric heights. NOAA's vertical datum transformation tool (NOAA, 2024c) is a widely used, open-sourced tool that is easily accessible and can perform vertical datum conversions.

Generate DEM

Spatial interpolation of ground classified points generated from the MLS survey is typically used to create a final gridded DEM product to support further coastal analyses. There are many GIS software options that can create a DEM, including ArcGIS, Quick Terrain (QT) Modeler, and Global Mapper. According to Smith, Rheinwalt, and Bookhagen (2019) and Gong et al. (2000), the accuracy of a DEM depends on the complexity of the terrain, land cover, spatial interpolation method, grid spacing, point density and distribution, measurement accuracy of the point cloud data, and accumulated uncertainty from every process thus far mentioned. In

the Smith, Rheinwalt, and Bookhagen (2019) study, the authors concluded that, in general, adequate spatial resolution, or the smallest acceptable grid-cell size, should not be interpolated at cell spacing greater than the average groundpoint spacing. One method of determining DEM cell size was developed by Hu (2003) and is defined by:

$$s = \sqrt{\frac{A}{n}} \tag{4}$$

where, grid-cell size s is computed using the number of points (n) within a given area (A). This method was applied in Langridge $et\ al.\ (2014)$ and Zhang $et\ al.\ (2021)$.

Lastly, the vertical RMSE of the DEM should be computed. This is mentioned by the ASPRS standards, edition 2 (ASPRS, 2024), which recommends that the vertical accuracy of the final survey product should be evaluated using checkpoints.

METHODS

This section outlines the empirical tests that were conducted to develop the optimized survey workflow for sandy beaches using mapping-grade MLS. The following experiments took place: sensor characterization and setup (lever arm measurement, LIDAR boresight calibration validation, camera boresight calibration validation, and ranging error characterization), quality assurance (INS initialization), processing and QC (strip adjustment validation and control layout and checkpoints), and point cloud classification (water-point classification). These experiments were essential to increase the accuracy and reliability of the point cloud data and resulting MLS system-derived DEM.

Sensor Characterization and Setup

This section describes the validation procedures and empirical tests conducted to contribute to sensor characterization and setup. Lever arm measurement, LIDAR boresight calibration validation, and camera boresight calibration validation are necessary procedures in this study because these values directly affect point cloud accuracy and alignment. Properly calibrated values ensure that the LIDAR data accurately reflects the orientation and position of the surveyed environment. Ranging error characterization is necessary to eliminate inaccurate points and minimize ranged-induced noise. Doing so increases point cloud fidelity and reduces uncertainty. These contribute to the collection of repeatable, accurate data.

Lever Arm Measurement

Although lever arm values are usually measured by the system distributor and sent to the user when a system is purchased, it is important to validate them. For this study, the system integrator manufactured and sent a rigid mount for the HiWay Mapper system components after the Snoopy A series had already been received by the authors. It was therefore essential for the research team to validate the lever arm estimates. The LIDAR and IMU body frame were integrated into the Snoopy A series. Because these lever arm values were already reliably measured by the system integrator, they were not manually measured, but adjusted during the

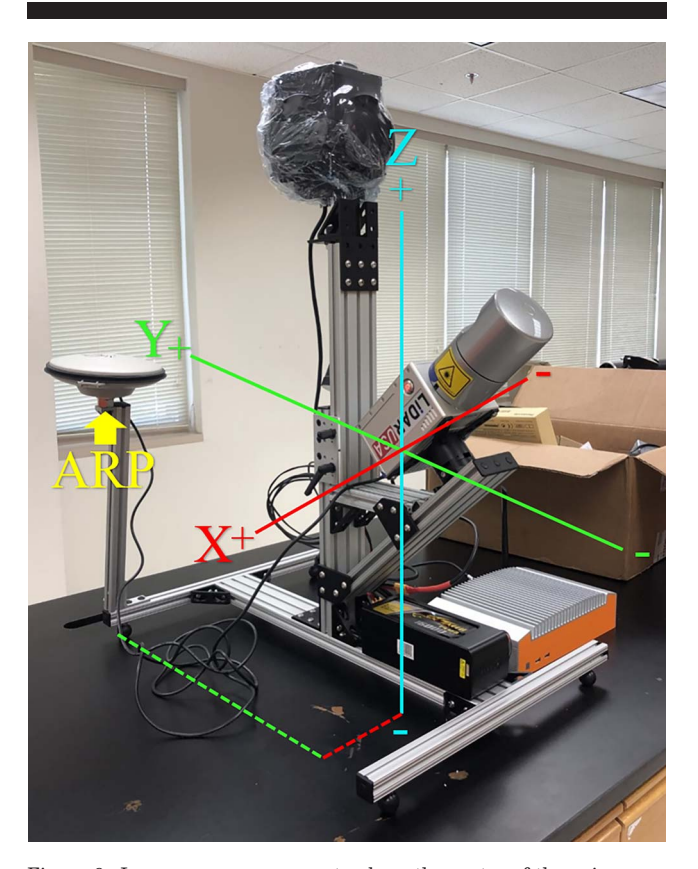


Figure 6. Lever arm measurement, where the center of the axis represents the IMU measurement point and the dotted lines represent X, Y, and Z value measurements that were made on a level, planar surface.

LIDAR boresight calibration validation process, described in the next section of this paper.

The research team then manually measured the lever arm offsets of the GNSS receiver to the IMU body frame origin. First, a smooth, level, planar surface was found. The rigid mount was placed on the surface with the LIDAR and GNSS receiver attached (Figure 6). To measure the height difference (the Z coordinate) between the GNSS antenna reference point (ARP) and the IMU, the heights of each respective component were measured and then differenced. Using a plumb bob, the planar surface was marked with the locations of the center of the GNSS ARP and the IMU measurement point. A perpendicular line was drawn away from the rigid mount, using a straight edge, and connected with a parallel line drawn from the lever arm. These were then measured to find the X and Y offsets of the receiver with respect to the IMU.

LIDAR Boresight Calibration Validation

Snoopy A series boresight calibration validation was completed because after many initial tests, the resulting point clouds contained object doubling, shifts in data, and misalignment between multiple passes. A boresight survey was completed in downtown Corpus Christi in a small parking lot adjacent to a large, flat wall with no windows. Three driving patterns were completed: two drive paths parallel to the wall,

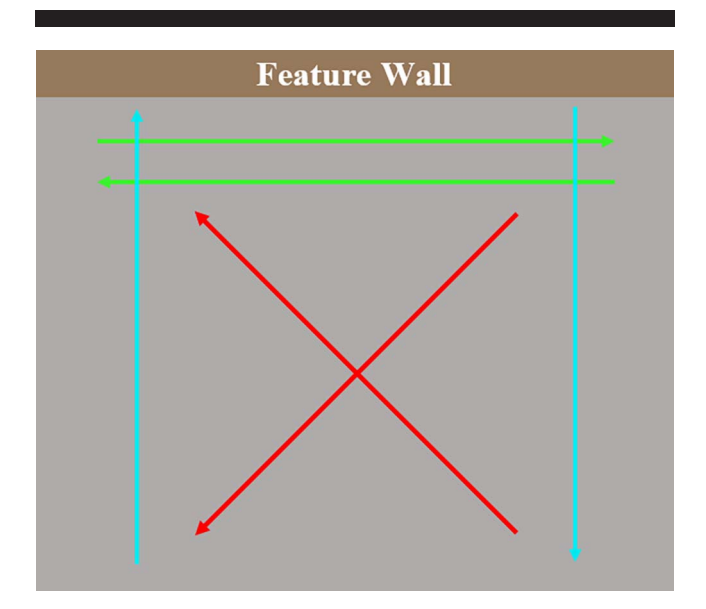


Figure 7. Lidar boresight calibration validation experiment design, which featured three driving patterns: perpendicular, parallel, and diagonal toward and from the feature wall.

two perpendicular to the wall, and two diagonal toward and from the wall, as seen in Figure 7. These patterns allowed the resulting point clouds of the feature wall to overlap, revealing misalignment in roll, pitch, and heading, whereas the ground revealed misalignment in elevation. The trajectory of the scan, generated in postprocessing, was used to create a point cloud using the former boresight values. Terrasolid (Helsinki, Finland) software was used to solve for boresight corrections using the following steps:

- (1) Separate the trajectory into independent drive paths, eliminating nonessential factors such as turns and unwanted points.
- (2) Clip the point clouds to eliminate trees, cars, and other unusable points.
- (3) Classify the point clouds.
- (4) Perform surface-to-surface matching, which triangulates the points related to each trajectory, compares overlapping points, and solves for heading, roll, pitch, and elevation differences *via* an iterative least-squares adjustment.

The resulting values provided corrections for roll, pitch, and heading, as well as LIDAR/IMU lever arm corrections, which were then applied to update the former values.

Camera Boresight Calibration Validation

An experiment to validate the Ladybug5+ camera boresight values was conducted in downtown Corpus Christi. To successfully perform the calibration, identifiable features needed to be visible in all six of the spherical camera's lenses. Because of this requirement, the area chosen had four tall buildings situated on an intersection with an overhead bridge connecting two of the buildings, as shown in Figure 8. The

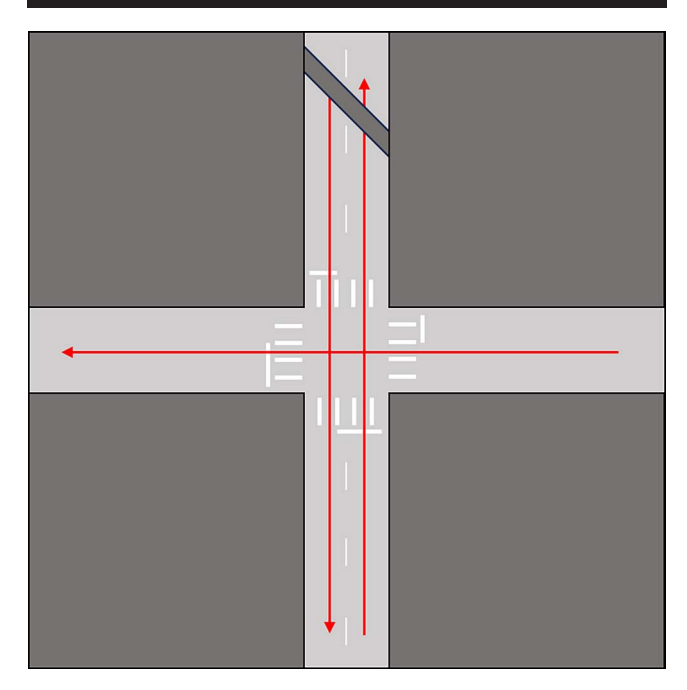


Figure 8. Camera boresight calibration validation experiment design, which took place at the intersection of four large buildings and featured a down-and-back drive with a perpendicular pass.

survey began in an open parking lot with few obstructions to initialize the system and reduce trajectory error due to satellite loss between buildings. The system was driven down and back on the main street, and a perpendicular pass was driven on a one-way cross street before completing the survey in the same parking lot in which it began. After the data were processed, a single frame was chosen from the imagery, and approximately 10 identifiable features, such as sidewalk corners, paint stripes, and signposts, were selected in each image. The corresponding points were selected in the processed point cloud. A least-squares algorithm then solved for translation and rotation errors, resulting in updated boresight angles and offsets in the IMU axes.

Ranging Error Characterization

In practice, the effective range of a LIDAR sensor is influenced by several factors, including the laser pulse energy, surface reflectance at the laser wavelength, incidence angle of the laser pulse, and other environmental factors. Most notably, ranging accuracy and precision for a LIDAR sensor tend to degrade after a certain distance. This ranging error propagates into the overall measurement accuracy and point cloud fidelity. Characterization of the ranging performance of a LIDAR scanner determines an effective range for planning and conducting surveys.

The Velodyne HDL-32E is a short-range sensor, with a manufacturer-reported effective range of 100 m. Chan, Lichti, and Belton (2013) reported an effective range for the Velodyne HDL-32E of 70 m, whereas Hauser, Glennie, and Brooks (2016) reported a practical range of 60 m. Because of conflicting reports, a range experiment was conducted to find

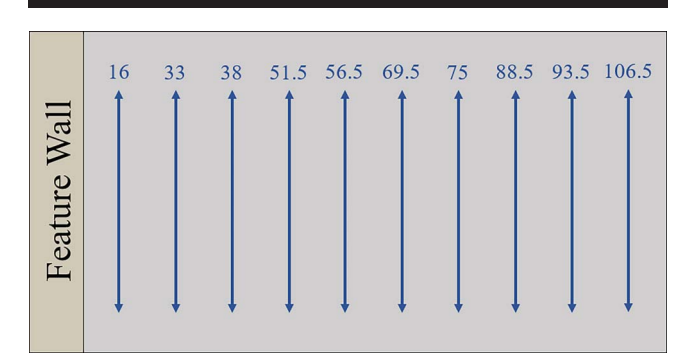


Figure 9. Layout of the range experiment in which 10 passes parallel to the feature wall were established from $16\ m$ to slightly more than $100\ m$, the reported effective range of the lidar.

the optimal range (*i.e.* maximum effective scanning distance) of the LIDAR scanner. This was conducted in a parking lot adjacent to a large building with a flat wall and no low windows on the TAMU-CC campus. This building was chosen because it had a surface on which an accurate plane could be modeled repeatedly with the MLS at varying distances from the system. This was used to assess the influence of range on the resulting measurements. The MLS was mounted on the roof of a vehicle, and 10 passes parallel to the building, from 16 to 106.5 m, were completed, collecting from both the left and the right sides of the sensor (Figure 9). A control survey was completed with a RIEGL VZ-2000i TLS (Horn, Austria), which collects up to 500,000 pts/s at a rate of 1.2 MHz and has a FOV of $100^{\circ} \times 360^{\circ}$, a range of up to 2500 m, and accuracy of 5 mm. The TLS and MLS scans were then clipped to a 4.4×1.3 m box on the feature wall around the same height as the MLS. The TLS point cloud was triangulated to create a best-fitting plane. A mean cloud-to-mesh distance was computed between the MLS point cloud and TLS plane by finding the distance between each point and the nearest mesh triangle (CloudCompare, 2023). The resulting statistics were evaluated to determine the effective range of the LIDAR system.

Quality Assurance

This section details the INS initialization experiment, which was a critical component of quality assurance. Proper INS initialization is critical for minimizing GNSS- and IMU-induced errors and ensuring the collection of high-quality MLS system trajectory data of system position and orientation during a survey. Because the largest errors in MLS surveys typically result from GNSS error and INS drift, a robust initialization procedure is key to mitigating these issues and more accurately georeferencing a given point cloud. The process not only maximizes positional accuracy but also reinforces the consistency and reliability of the workflow (CALTRANS, 2018; Lim et al., 2013; Olsen et al., 2013).

INS Initialization

Initialization of the MEMS-IMU used in this study was recommended by both the MLS system integrator and the INS distributor. LiDARUSA (2022) recommended statically initializing the INS in the direction of travel for at least a few

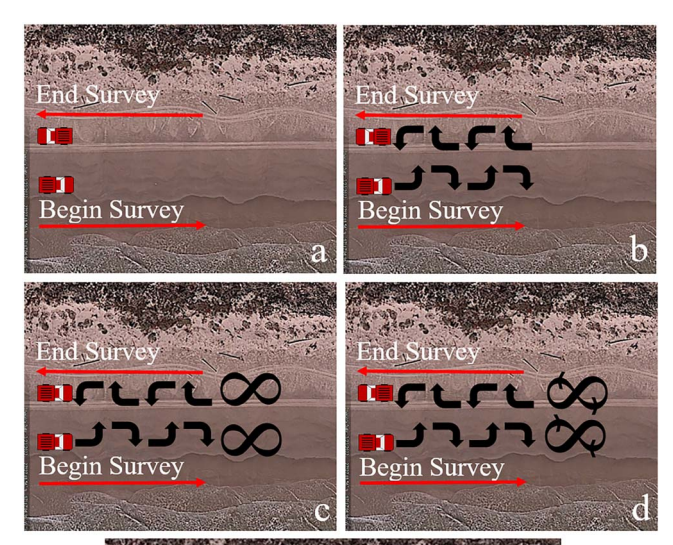




Figure 10. INS initialization experiment driving procedures: (a) 5-minute static; (b) 5-minute static and two LH plus two RH turns; (c) 5-minute static, two LH plus two RH turns, and two loose F8s; (d) 5-minute static, two LH plus two RH turns, and two F8s in both directions; and (e) 5-minute static, four LH plus four RH turns, and four F8s in both directions.

minutes. Kinematic initialization should follow, which includes driving in a straight line for 30 seconds, followed by a right-hand (RH) turn–left-hand (LH) turn sequence at a speed of more than 8 km/h. Similarly, the NovAtel user manual (NovAtel, 2013) advised users to first remain static. Then, they should perform figure-eight (F8) motions iteratively, stopping for at least 5 seconds after each iteration. This process must be continued for 3 minutes, with initialization movements mirrored after completion of a project. Glawe (2016) recommended initializing 5 minutes before and after data collection to increase the accuracy of a small survey. Because of conflicting recommendations, an INS initialization experiment was conducted to verify the complexity of procedures necessary to properly align the MLS system for surveying sandy beaches.

A rigorous INS initialization experiment took place on the TAMU-CC campus. Five initialization procedures were tested, gradually increasing the level of dynamic driving. Each method was completed before a short survey was conducted, and the reverse procedure was performed afterward. The INS was powered off for 5 minutes between each procedure. The five procedures were as follows (Figure 10):

- (1) 5-minute static
- (2) 5-minute static and then two LH plus two RH turns

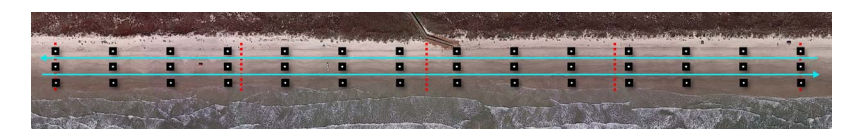


Figure 11. Survey setup for phase 3, where three GCPs were laid every 50 m and five topographic checkpoint transects (shown as red dotted lines) were spaced every 200 m. The survey consisted of two passes (shown as solid blue lines): one near the dune and one near the shore.

- (3) 5-minute static, two LH plus two RH turns, and then two loose F8s
- (4) 5-minute static, two LH plus two RH turns, and then two F8s in both directions
- (5) 5-minute static, four LH plus four RH turns, and then four F8s in both directions

The resulting scans were processed using PPK with a fixed, localized GNSS base station located and maintained on the TAMU-CC campus. The trajectories for each survey were processed using NovAtel's Waypoint Inertial Explorer, and its' GNSS+INS QC group of plots were used to compare positional accuracies. These included estimated position accuracy, estimated attitude accuracy, IMU-GNSS position misclosure, and PDOP plots. These plots showed qualitative data of the MLS system's position, attitude (*i.e.*, roll, pitch, and heading), difference between the GNSS and INS positions, taking into consideration estimated position accuracy spikes due to poor satellite geometry.

Data Processing and Quality Control

This section describes the experiments conducted to develop data processing and QC. The data processing experiments validated the trajectory processing method and strip adjustment to ensure their applicability to this study. In addition, these experiments provide detailed guidelines for coastal researchers and engineers to assess whether these methods are suitable for their own systems and coastal environments. The control layout and checkpoint experiment offered rigorous analyses to identify optimal GCP spacing and configuration for repeat surveys. Collectively, these procedures establish a systematic and repeatable approach to data processing and QC to provide accurate results.

The experiments conducted in data processing and QC and postprocessing, presented in the next section, were based on a single survey conducted on North Padre Island, Texas (Figure 1), on an 805-m stretch of beach. In this survey, a local, centralized base station was established and two overlapping scan lines were performed: one closer to the dune and one closer to the shoreline (Figure 11). The aims of this survey were to (1) determine the difference between loosely and tightly coupled trajectory processing methods, (2) assess the applicability of strip adjustment, and (3) determine the effects of GCP target spacing and geometry.

A GCP layout experiment was conducted to find a balance between minimizing the number of control points and achieving high-quality data. A series of GCPs were laid on the beach to improve georeferencing and positional accuracy of the MLS survey, resulting point cloud data, and for accuracy assessment. They were made of 0.6×0.6 m plywood with a black painted surface and a 122-mm white circle fitted with a 50-mm reflective sticker. A total of 42 targets were used, with 3 targets laid every 50 m. Five natural ground transects were collected for use as checkpoints from the waterline to the dune toe and spaced every 200 m alongshore (33 points total). The ground targets and topographic points were georeferenced using a local RTK GNSS receiver connected to the Texas Department of Transportation Real-Time Network (RTN) with an epoch collection rate of 5 seconds. The cross-shore elevation transects (i.e. topographic point data) were collected with an epoch collection rate of 3 seconds, from the waterline to the dune toe, and were used for vertical accuracy assessment. See Figure 11 for an example of the survey layout.

Data Processing

Data processing experiments were conducted to identify the most effective data processing procedures for deriving accurate trajectories and georeferenced point clouds from the MLS system data. Trajectory processing played a critical role for ensuring accurately georeferenced point cloud data. Strip adjustment validation assessed the impact of a strip adjustment, ensuring the alignment and accuracy of the final point cloud.

Trajectory Processing. Trajectory processing was completed in Inertial Explorer using both loosely and tightly coupled processing methods, with combined forward and backward solutions. To compare the performance of the two methods, the Waypoint GNSS+INS QC group of plots in Inertial Explorer were evaluated. This exported 18 plots that assessed the trajectory accuracies, estimated attitude accuracy, position difference between the forward and the backward solutions, QC, and IMU information (NovAtel, 2024a). After a method was chosen, the trajectory was used to generate a point cloud.

Strip Adjustment Validation. Strip adjustment validation was performed in Terrasolid using the processed trajectory, trajectory accuracy file, and point cloud. The trajectory was first split to remove the INS initialization maneuvers and turnarounds. Then, surface-to-surface matching triangulated the point cloud surface of each strip. Afterward, all overlapping LIDAR points and surfaces were compared. Lastly, an iterative least-squares adjustment was performed to solve for heading, roll, pitch, and elevation differences and to align the strips. Vertical RMSE was computed for each point cloud using the cross-shore topographic transects, where the vertical offset of each topographic checkpoint was compared for each strip. After, the point clouds, before and after strip

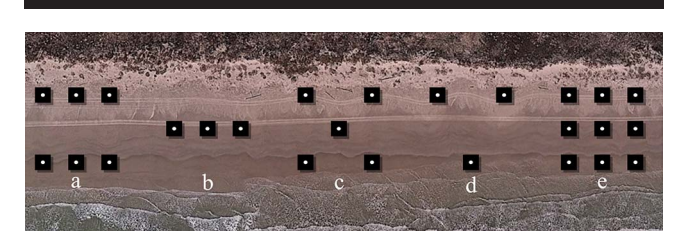


Figure 12. Five GCP configurations evaluated in the GCP experiment: (a) outer, (b) inner, (c) outer and inner, (d) alternate, and (e) all.

adjustment, were visually compared by extracting crossshore elevations. These were both used to assess the strip adjustments' effectiveness on vertical accuracy and on the attitude of the point clouds.

Control Layout and Checkpoints

Several GCP configurations and distances were analyzed and applied to both a strip-adjusted and a non–strip-adjusted point cloud using a least-squares adjustment. Five GCP patterns, as pictured in Figure 12, were evaluated at distances of 100, 200, 300, 400, 500, and 600 m, with 21 targets evaluated and 21 used as checkpoints. Vertical error was computed using lasTool's lascontrol module which by default, for each checkpoint, computes a 15×15 m TIN surface from the MLS point cloud. Each checkpoint is then compared to the TIN surface. The average vertical error, RMSE, and standard deviation of each configuration were calculated using the natural ground transects and targeted checkpoints.

Postprocessing

This section details the point cloud classification experiment performed in postprocessing.

Point Cloud Classification

Point cloud classification, including noise removal and ground point classification took place prior to the water point classification experiment. These steps are described in detail below in the case study. It is important to note that these steps create a clean set of ground point data which significantly affect the quality of the final DEM and resulting RMSE. If not implemented properly, these methods may fail to eliminate unwanted points and features, introducing false surfaces to the DEM. Therefore, it is essential to thoroughly inspect the data during these steps to ensure that nonground points are adequately removed while preserving ground features. For repeat coastal surveys, consistent classification settings and methods can be applied to maintain uniformity across datasets and optimize both accuracy and overall data quality.

Water Point Classification. Water point classification Was conducted to identify the most effective method for this project with the tools available to the authors. Even though every survey took place as close to low tide as possible, it was important to remove noise and inaccurate points to maximize beach coverage. The first method tested was manual shoreline delineation, which was deemed too time intensive and

Table 1. Lever arm offsets before and after manual lever arm measurement.

| | Before (m) | After (m) |
|---|------------|-----------|
| X | -0.206 | -0.243 |
| Y | 0.503 | 0.503 |
| Z | 0.127 | 0.034 |

user specific and could likely lead to bias. The second method generated a lowest elevation contour. This was applied to initially clip the water, and manual delineation was used to remove the rest of the points by following the contour. Lastly, a discrete attribute analysis tool in QT Modeler was used to apply high- and low-intensity bounds on the point clouds. The high-intensity bounds masked points from breaking waves, and the low-intensity bounds masked points from water absorption. This created a distinct waterline, which was then used to manually filter the remaining water points.

RESULTS

This section presents the results from the field experiments employed to form an optimized survey workflow for sandy beach corridor mapping using mapping-grade MLS systems.

Sensor Characterization and Setup

The objectives of this phase were to ensure that MLS system errors resulting from incorrect lever arm values, LIDAR and camera boresight values, and ranging were minimized. Before conducting and developing this step, the derived point clouds contained object doubling and misalignment, indicating that the system values required adjustment and validation.

Lever Arm Measurement

The GNSS lever arm values with respect to the IMU were hand measured to ensure their accuracy and minimize potential errors. During this process, a discrepancy was observed between the manually derived values and the previously estimated values. This was most notable in the Z component, which differed by 9 cm, as shown in Table 1. This deviation was significant, because inaccurate lever arm measurements propagated significant errors into the final point cloud. These values were incorporated into the trajectory processing for the subsequent LIDAR boresight calibration. This adjustment was necessary to ensure that the calibration results were reflective of the true sensor alignment and not skewed because of incorrect offset parameters, ultimately preserving data quality and measurement precision.

LIDAR Boresight Calibration Validation

The LIDAR boresight values were validated using a boresight calibration procedure. The process corrected the original values by solving misalignment in roll, pitch, and heading. Those adjustments were integrated with the existing values, enhancing point cloud fidelity and reducing errors. In addition, LIDAR to IMU lever arm corrections were calculated as part of the boresight calibration. GNSS to IMU lever arm corrections were also refined in Inertial Explorer during processing. In combination, these values contributed to the overall accuracy of the data and they significantly reduced noise and increased visibility of the resulting point clouds, as shown in Figure 13. The image illustrates that before lever arm measurements and boresight

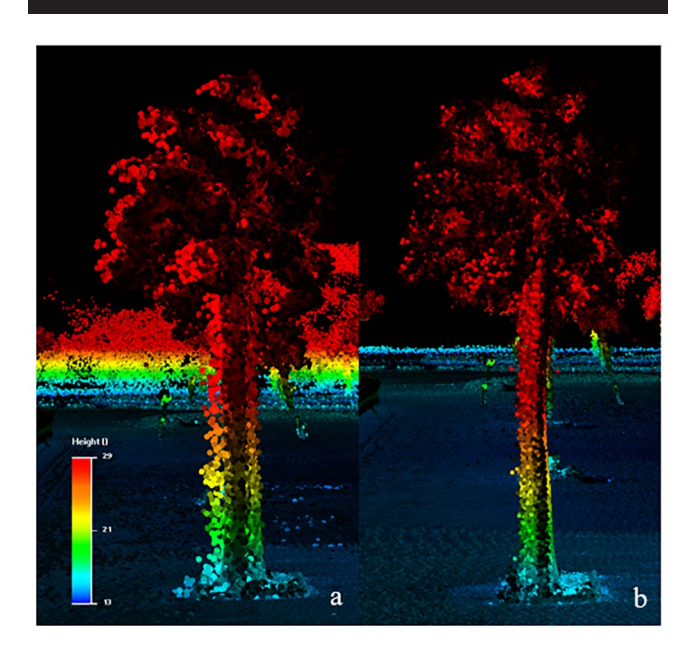


Figure 13. Visualization of an MLS system-derived point cloud (a) before and (b) after lever arm measurement and lidar boresight calibration validation.

calibration, object doubling was present. After the adjustments were made, a cleaner point cloud was presented. This procedure resulted in significant noise reduction and enhanced point cloud clarity. The validation authenticated the need to verify and refine lever arm and boresight values in this study.

Camera Boresight Calibration Validation

Camera boresight values were verified by performing camera boresight calibration to reduce colorization errors. It was initially noted that there was a significant density of blue pixels assigned to the highest points, including on the tops of dunes and powerlines, as pictured in Figure 14. The camera boresight calibration's purpose was to minimize the concentration of falsely colorized points. After performing the procedure, the updated values remained largely unchanged, indicating relatively stable values. This process also confirmed that falsely colorized points were still present for this particular system when using the calibrated camera boresight values. This resulted from the imagery containing a high concentration of blue pixels from the sky, which were interpolated on the tallest objects. However, this experiment was necessary for verification of the camera boresight values relative to the IMU and lidar sensor orientation and to reduce colorization errors. Performing an image registration and fine alignment to the resulting point cloud data using more specialized tools or software could potentially better align the camera frame of reference to the lidar frame of reference for tighter colorization.

Ranging Error Characterization

The range experiment assessed the deviation of MLS-derived points at 10 varying distances from the LIDAR scanner to a reference surface (a planar wall). A TLS survey served as the control and was used to create a best-fit plane. To determine the effective range of the LIDAR scanner, the



Figure 14. Example of a colorized point cloud.

mean distance and standard deviation of the point cloud to the plane were assessed, shown in Table 2. Based on those values, it was determined that the effective range of the Velodyne HDL-32E used in this study was 70 m. At distances farther than 70 m, the mean distance and standard deviation were more variable. Determining this range significantly reduced ranging error imprecision by applying it as a maximum distance filter. In addition, it informed decision making by accounting for range-induced errors in scan line planning. This helped to optimize the workflow through the improvement of survey planning and reliable point cloud products.

Quality Assurance

Activities that are included in quality assurance include, but are not limited to, proper knowledge of the terrain, extent and width of the beach to be surveyed, weather and water conditions, and GNSS conditions. Although most information is easily obtained, an INS initialization experiment was conducted to improve the quality of the MLS system-derived data.

INS Initialization

The INS initialization experiment evaluated five initialization procedures, varying in intensity. The trajectory quality of each procedure was quantified and compared using Inertial Explorer. The trajectory plots that were assessed included the Waypoint GNSS+INS QC plots, a group of plots within Inertial Explorer conveniently selected for QC. The analyses focused on assessing the estimated standard deviation and attitude and IMU-GNSS position misclosure, taking PDOP into account for misclosure spikes. It was found that the trajectory qualities of driving procedures 2 to 5 (see Figure 10) were similar. The standard deviations decreased in

Table 2. Range experiment results computed using a cloud-to-mesh distance measure (MLS point cloud to TLS control plane, respectively).

| Scan Line | Distance from Wall (m) | Mean Distance (m) | Standard Deviation (m) |
|--------------|------------------------|----------------------|---------------------------|
| 1 | 16 | -0.017 | 0.030 |
| 2 | 33 | -0.024 | 0.422 |
| 3 | 38 | -0.023 | 0.052 |
| 4 | 51.5 | 0.002 | 0.049 |
| 5 | 56.5 | -0.011 | 0.411 |
| 6 | 69.5 | -0.006 | 0.056 |
| 7 | 75 | 0.010 | 0.072 |
| 8 | 88.5 | -0.017 | 0.078 |
| 9 | 93.5 | -0.016 | 0.064 |
| 10 | 106.5 | 0.033 | 0.052 |

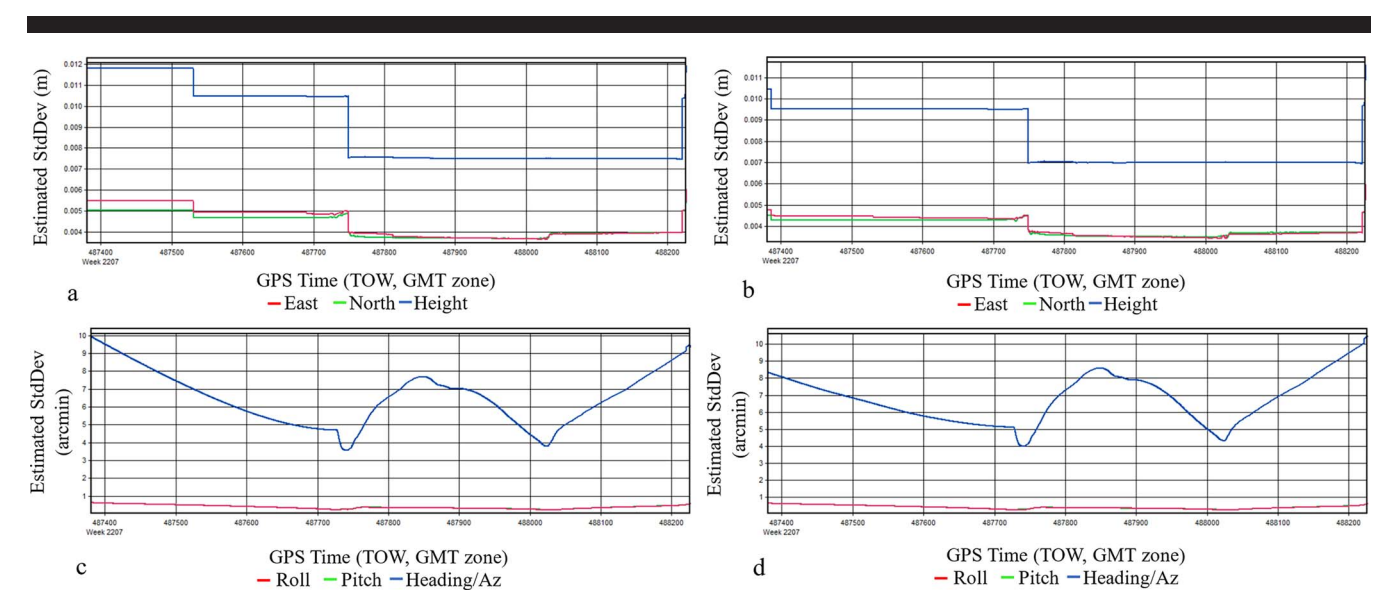


Figure 15. Comparison of the estimated position accuracy (a and b) and estimated attitude accuracy (c and d) between loosely coupled (a and c) and tightly coupled (b and d) trajectory processing (plots were created in Inertial Explorer).

less time than procedure 1 and the estimated IMU-GNSS position misclosure mostly remained within ±0.01 m. Procedure 1 obtained the overall worst estimated values, taking more time for the standard deviation to decrease and an IMU-GNSS misclosure of over 0.03 m in some cases. This indicated that without dynamic driving the IMU and GNSS took a longer amount of time to align. This would likely increase the likelihood and amount of time taken for the IMU to drift due to the lack of dynamic maneuvers in beach surveying. This inferred that the static driving procedure 1 was not sufficient to properly align the INS before the survey took place. The rest of the results determined that an elaborate driving procedure was not required, but a small amount of dynamic driving was needed. Therefore, driving procedure 3 was implemented in this study because F8s provided a directional shift, which doesn't occur often in an alongshore coastal survey.

Data Processing and Quality Control

The purpose of data processing and QC was to optimize postsurvey procedures for minimizing trajectory and point cloud errors and evaluate the vertical accuracy of the point cloud. This section presents the results of data processing and the control layout and checkpoints experiments.

Data Processing

The results presented in data processing evaluated the trajectory solution and assessed the quality of strip adjustment, serving as QC measures within data processing.

Trajectory Processing. Trajectory processing was evaluated for a survey using loosely and tightly coupled methods, with combined forward and reverse solutions. The trajectory accuracy plots in Inertial Explorer were evaluated to compare the quantitative differences between these two methods. Most didn't have notable differences. The estimated position accuracy and

estimated attitude accuracy plots (Figure 15) did display qualitative variability. Loosely coupled processing (Figure 15a,c) obtained slightly higher standard deviation values than tightly coupled processing (Figure 15b,d), indicating that tightly coupled trajectory processing was a better method for this project. These results suggest findings that aligned with the project goals, which aimed to reduce errors to achieve the highest-quality data.

Strip Adjustment Validation. Strip adjustment validation evaluated the effectiveness of a strip adjustment. This was accomplished by computing the RMSE of the surveys as a whole and at individual checkpoints, comparing the difference. Cross-shore transects were compared for visual alignment, an example of which is pictured in Figure 16. The cross-section visuals and RMSEs indicated that the strip adjustment was mainly applied at farther ranges from the system, particularly in the dunes. In addition, there was elevation variability in the dunes, which could result from the presence of dense, low-lying vegetation. The cumulative vertical RMSE shown in Table 3 demonstrated that strip adjustment increased the vertical accuracy of the coastal sandy

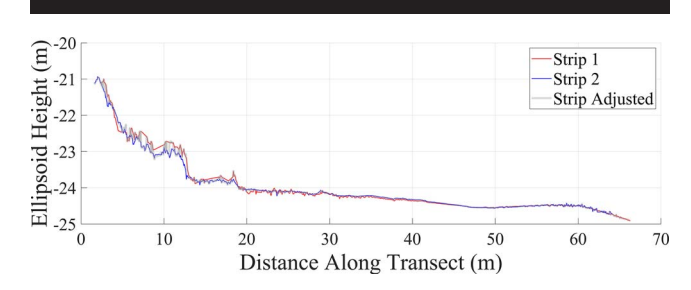


Figure 16. Cross-shore transect displaying two point clouds before (strip 1 and strip 2) and after strip adjustment.

Table 3. Average RMSE for each strip adjustment method as computed with targeted and topographic checkpoints.

| | RMSE (m) | |
|--------------------------------------|----------------|----------------|
| | Targeted | Topographic |
| Not strip adjusted Strip adjusted | 0.017 0.016 | 0.036 0.034 |

beach survey, but the reduction in RMSE was not significant. What was noteworthy was the alignment of the dunes, revealing that strip adjustment reduced noise and variability. This implied that this step was crucial in the workflow to reduce uncertainty in the dunes and align overlapping strips to increase the fidelity of a final DEM product.

Control Layout and Checkpoints

The GCP experiment evaluated the vertical RMSE for five GCP configurations at six varying intervals to identify which had the greatest influence on reducing vertical RMSE. The RMSE of the unadjusted point cloud was 0.12 m, as computed with topographic checkpoints. Figure 17 displays the RMSE of the GCP patterns applied as calculated with targeted checkpoints (Figure 17a) and natural ground topographic checkpoints (Figure 17c). It also shows the RMSE of stripadjusted point clouds with the GCP patterns applied as calculated with targeted checkpoints (Figure 17b) and natural ground topographic checkpoints (Figure 17d). For all cases, the RMSE trends downward as the GCP frequency increases, reaching as low as 0.02 m. In general, the inner pattern yielded the worst results, with the outer-and-inner pattern also underperforming. The RMSE values also varied from

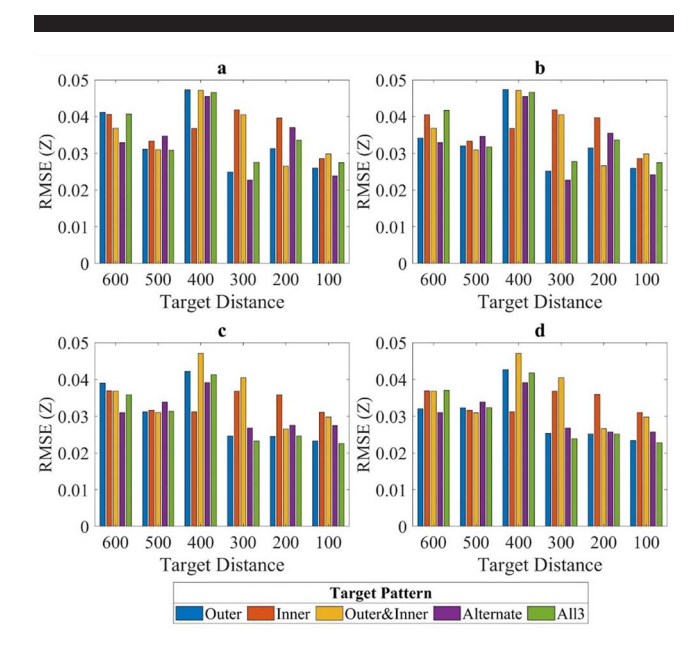


Figure 17. Point cloud accuracy of five patterns of GCP placement: (a) RMSE of only GCPs as calculated with targeted checkpoints, (b) RMSE of strip-adjusted point clouds with GCPs as calculated with targeted checkpoints, (c) RMSE of only GCPs as calculated with topographic checkpoints, and (d) RMSE of strip-adjusted point clouds with GCPs as calculated with topographic checkpoints.

Table 4. Average RMSE for each GCP experiment pattern as computed with targeted and topographic checkpoints.

| | Only GCPs (m) | | $Strip\ adjusted + GCPs\ (m)$ | |
|-----------------|---------------|-------------|-------------------------------|-------------|
| | Targeted | Topographic | Targeted | Topographic |
| Outer | 0.033 | 0.030 | 0.032 | 0.030 |
| Inner | 0.036 | 0.033 | 0.036 | 0.033 |
| Outer and inner | 0.035 | 0.033 | 0.035 | 0.033 |
| Alternate | 0.032 | 0.030 | 0.032 | 0.030 |
| All | 0.034 | 0.029 | 0.034 | 0.030 |

0.022 to 0.047 m, displaying a variability of more than 0.02 m, with lower RMSEs at intervals between 100 and 300 m.

For further analysis, the average RMSE of each pattern and method was computed, as displayed in Table 4. This revealed that the outer, alternate, and all patterns yielded similar accuracies, with strip-adjusted point clouds holding slightly higher accuracies. However, the average RMSE did not display as much variability as in Figure 17. Delving further into the feasibility of laying and georeferencing each pattern with an accompanying checkpoint over a long beach corridor survey, the all and outer patterns would result in surveys that would require more time and targets. Therefore, the alternate geometry was chosen for use in future studies. This pattern essentially reached the same accuracies, required fewer targets, and resulted in shorter surveys than the other patterns.

The RMSE also decreased as spacing intervals became smaller. In general, the highest average RMSE values occurred at 600 m intervals, while the lowest were observed at 100 m intervals. Although all spacing intervals resulted in RMSEs below 5 cm, those at and below 300 m consistently achieved RMSEs around 3 cm. Given the higher vertical accuracy of the selected alternate geometry at smaller intervals, 200 and 300 m were chosen for implementation in future studies, depending on survey length and the number of ground targets available. For the MLS system used in this study, GCPs were placed every 200 m for surveys less than 4.5 km, 300 m for surveys greater than 4.5 km, and within 10 m from the drive path. For surveys greater than 10 km, the GCP spacing would need to be revisited. The number of GCPs at each interval depended on the number of scan lines needed as represented by:

$$N_{GCP/interval} = N_{SL} - 1 \tag{5}$$

where, N_{GCP} is the number of GCPs needed per interval and N_{SL} is the number of scan lines at each interval (see equation 2 to compute N_{SL}). For every interval, there was also an accompanying targeted checkpoint to be used in vertical accuracy assessments and serve as a safeguard lest a blunder occur when georeferencing the GCPs. Lastly, at least five evenly distributed natural ground topographic transects were collected with each survey.

Finding an effective GCP network geometry and spacing for the sandy beach environment was an important component of the survey workflow for producing repeatable and accurate point cloud data with the mapping-grade system evaluated in this study. Compared to direct georeferencing solutions without inclusion of GCPs, use of GCPs resulted in a reduction of vertical RMSE in the majority of surveys

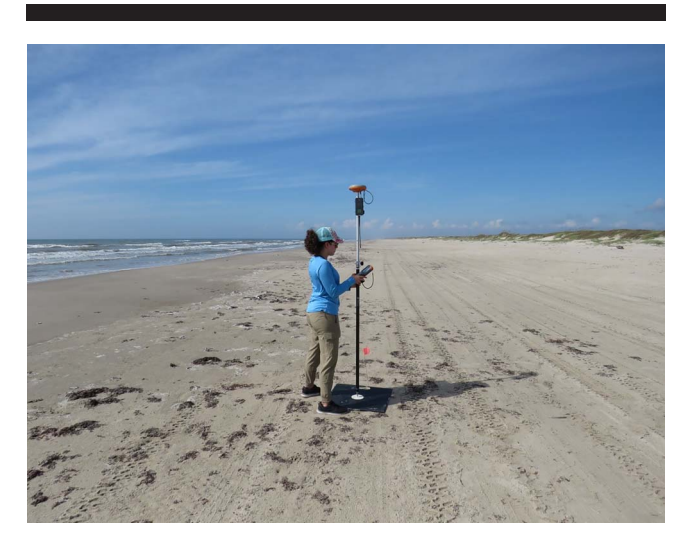


Figure 18. Visualization of Malaquite beach and example of target type and GCP placement.

evaluated in this study relative to checkpoints. In some cases where high vertical error was observed in certain segments of the survey after strip adjustment, GCPs helped to stabilize the bias and constrain the point cloud solution.

Summary

The empirical tests successfully aided the development of an optimized survey workflow for sandy beach corridor mapping using a mapping-grade MLS system. An approach for sensor calibration was essential, revealing that accurate lever arm measurement and boresight calibration minimized point cloud errors, particularly object doubling and misalignment. An effective range of 70 m was established to reduce ranging errors and thus improve data quality. Camera calibration validated the existing measurements and ensured consistency in data processing and point cloud colorization. INS initialization stressed the need for controlled initialization procedures to limit INS errors. Postprocessing validation found that tightly coupled processing minimized trajectory errors, and strip adjustment validation stressed the need for the alignment of multiple passes. The evaluation of a GCP network proved critical for adjusting and limiting vertical error of the resulting point clouds. Collectively, the results enhanced the vertical accuracy of sandy beach surveys and improved data fidelity.

CASE STUDY: MALAQUITE BEACH AT PAIS

PAIS is located on North Padre Island, a barrier island that is bordered by the Laguna Madre estuary on the west and the Gulf of Mexico on the east. This 113-km island is the longest stretch of undeveloped barrier island in the world and ranges from 0.8 to 4.8 km in width (Bracewell, 2023; Cooper et al., 2005). It is also the secondary nesting beach of the Kemp's ridley sea turtle (Lepidochelys kempii), the most endangered sea turtle species in the world (Shaver et al., 2016). The north end of the beach, where Malaquite beach is located (Figures 1 and 18), is characterized by a gently

sloping sand beach (Weise and White, 2007). It is relatively flat with broad, shallow, outspread cusps consisting of fine sand, which is primarily made up of quartz. It is a low-energy coastline, with wind-driven tides that are more influential than astronomical tides. As a Gulf-facing beach, PAIS's beach and dune morphology are mainly driven by tides and winds, along with tropical storms, hurricanes, and other events (Bracewell, 2023). Waves create longshore drift of sediment and are typically less than 1 m high but can reach over 2 m during strong storms (KellerLynn, 2010; Pendleton et al., 2004). A beach-adjacent dune ridge typically ranges from 6 to 12 m in height. Shoreward of the dune ridge lies a series of coppice mounds, usually less than 1 m high (Weise and White, 2007). According to Weise and White (2007), the dunes in this area have been reported to migrate up to 26 m/y, with an average movement of approximately 10.5 m/y. In addition, according to Bracewell (2023), relative sea-level rise averages about 4.5 mm/y on Malaquite beach.

Two MLS surveys were conducted along a 4 km northern section of Malaquite beach on 26 July and 22 September 2022. The data collection and processing were conducted following the survey workflow developed in this work, as previously described. The purpose of these surveys was to assess the vulnerability of Kemp's ridley sea turtle nesting habitat; thus, it took place in areas of documented nests along the sandy beach shoreline. Malaquite beach is a pedestrian only beach, and permit authority granted the authors vehicle access to conduct the surveys. The survey procedures and data processing steps presented in this case study follow those of the 22 September survey, whereas the results presented below show examples from both surveys. No imagery was collected because of system complications.

The purpose of this case study was to showcase the utilization of the survey workflow developed and optimized for the mapping-grade MLS used in this study. It is organized by phase to demonstrate real-world survey parameters and how they relate to the four-phase process. Phases 2 to 4 are discussed because the phase 1 parameters were described earlier and take place before planning and conducting a coastal survey. Analyses of the surveys demonstrate the types of data that can be extracted from the bare-earth DEMs. The software and websites used in the case study are listed in Table 7.

Quality Assurance

Prior visitation to Malaquite beach was essential for the field crew to organize and execute the survey efficiently and effectively. Key parameters were collected during this preparatory stage to facilitate the planning and implementation of the survey, ensuring the collection of quality data.

Driving Parameters and Scan Settings

The scanner settings, which are unique to the system, were as follows: (a) a frame rate of 20 Hz was consistently used in this study, and (b) single return mode was used to maximize the scan range and ensure stronger returns. The beach surveyed was narrow, about 60 m wide. For ample overlap and coverage (particularly for data occlusion behind the vehicle), two passes of the site were completed at 50% minimum

sidelap. On a wider beach, the D_{SL} for this system would be 105 m. However, due to the narrow nature of the beach, D_{SL} was 40 m. The speed limit immediately north of the closed beach was 6.7 m/s. To provide ample ground coverage and for animal and pedestrian safety, a maximum driving speed of 4.5 m/s was implemented.

Beach Conditions

Metocean conditions on 22 September at the time of survey were as follows: the temperature was 35°C, with a perceived temperature of 40°C, and 69% relative humidity. Wind speed was 2.2 m/s NE with wind gusts of 4 m/s (AccuWeather, Inc., 2025). The wind direction with respect to the study site was cross-shore, and the significant wave height was 0.61 m as found by hindcast data downloaded from the Wave Information Study (WIS) station ST73035 (USACE, 2024), closest to the study site. Tide information was found on NOAA's tides and currents website (NOAA, 2024b). High tide was 0.26 m NAVD88 at 0358 CST, low tide was -0.11 m NAVD88 at 1947 CST, and MHW for this location was 0.314 m NAVD88. The survey was conducted in the afternoon to be as close to low tide as possible while adhering to National Park Service work hours, as required by the permit.

GNSS Base Station and GNSS Conditions

A local GNSS base station was established in the center of the site, about 2 km from each end of the survey. It collected at 1 Hz with a 10° cutoff angle for at least 4 hours, as recommended by Gillins, Kerr, and Weaver (2019). According to Trimble GNSS Planning, 137 of 140 satellites were active, with 31 GPS and 22 GLONASS satellites available throughout the course of the day. The vertical dilution of precision was 0.74. The base station data was used for correction of the MLS sensor trajectory and for collecting RTK points for ground control and checkpoints.

Data Processing and Quality Control

The raw data were downloaded immediately upon return from the field from the GNSS receiver, data collector, and LIDAR scanner. Although the data can be processed the next day, the authors waited 2 weeks for the precise ephemerides to get the most accurate GNSS solution possible.

Control Layout and Checkpoints

To increase the readability of this section, the control layout and checkpoints section is presented before data processing. During the survey, 21 targets were laid in pairs every 200 m alongshore and georeferenced with a GNSS rover collecting at 5-second epochs receiving RTK corrections from the local GNSS base station established at the study site as described above. They were labeled in the data collector, following the recommended alternate GCP pattern (Figure 12), according to type (GCP or checkpoint). A total of 11 targets were labeled as GCPs, whereas the other 10 were labeled as checkpoints. In addition, topographic checkpoints were collected in transects every 300 m alongshore using 3-second epochs. A total of 93 topographic points from the shoreline to the dune toe were collected.

Table 5. Average RMSE of the Malaquite beach surveys before and after strip adjustment + GCPs and the final, bare-earth DEM.

| | RMSE (m) | | |
|--------------------------|--------------|-------------------|--|
| | 26 July 2022 | 22 September 2022 | |
| Not strip adjusted | 0.038 | 0.036 | |
| $Strip\ adjusted + GCPs$ | 0.037 | 0.034 | |
| DEM | 0.039 | 0.037 | |

Data Processing

Before processing the LIDAR data, the GNSS receiver independent exchange format file was submitted to the NGS Online Positioning User Service (OPUS; NGS, 2022) to postprocess the GNSS base station data. The processed GNSS base station was then used to adjust the RTK survey points used for establishing GCP targets and checkpoint data collection. The base station observation file and updated coordinates were then uploaded into Inertial Explorer navigation processing software to process the MLS sensor trajectory. This was processed using a tightly coupled method with combined forward and backward solutions. The trajectory accuracy was evaluated using Inertial Explorer's Waypoint GNSS+INS QC group of plots. These indicated that GNSS-INS errors were minimized to approximately ± 1 cm vertical, and the forward and backward processing agreed. The point clouds were then generated in ScanLook PC, LidarUSA's point cloud processing software, using minimum and maximum distance filters of 2.5 and 70 m, respectively, to remove truck bed and long-range points. Strip adjustment was then performed in Spatial Explorer to align the two passes, and GCPs were integrated in the correction.

Vertical Error Quantification

The checkpoints were imported into Spatial Explorer, a lidar acquisition, QC, and post-processing software, to assess the vertical error of the survey before and after strip adjustment. This was to ensure that no blunders took place and the strip adjustment worked correctly. Afterward, the point cloud was exported, and lascontrol, a module within LAStools' software, was used to compute the vertical RMSE using the RTK topographic ground-truth points. The accuracy of both surveys can be viewed in Table 5.

Post-Processing

The processed point cloud was then classified to contain only ground points and converted to NAVD88 before a bare-earth DEM was generated.

Point Cloud Classification

The point clouds were classified for noise and nonground points before water was removed. Noise classification was conducted using lasnoise, an LAStools module, which identified and flagged isolated clusters of 50 points within a 1 m³ space. Ground points were classified using LAStools' lasground module with a step size of 0.4, a spike tolerance of 0.5, and the not-airborne setting to refine the classification. These parameters were selected to balance accurate ground detection while minimizing misclassification of non-ground features and were first tested on a small section of beach with bollards, vehicles, and pedestrians. Despite these filtering steps, a significant presence of seabirds along the shoreline

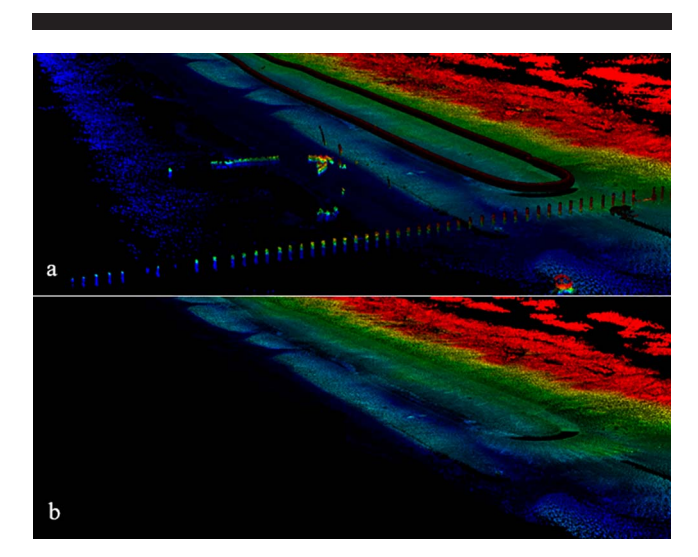


Figure 19. Visual of (a) before and (b) after noise removal, ground-point classification, and water-point classification.

and wave runup area introduced challenges in this survey. The high density of birds in some locations resulted in certain clusters being misclassified as ground due to their contiguous nature. To address this, residual points were manually reviewed and reclassified in QT Modeler point cloud processing software after the initial noise and ground classification. The discrete attribute tool in QT Modeler was used to highlight points with intensity values between 12 and 84, effectively isolating water. The shoreline was then manually delineated. This classification step helped refine the dataset by removing non-ground features that were not adequately filtered by the automation process. Figure 19 illustrates the point clouds before and after filtering and classification, demonstrating the effectiveness of the applied workflow.

Vertical Datum Conversion

The point clouds were converted to NAVD88 using the lasv-datum module from LAStools. The necessary GEOID18 geoid

model, developed by NGS for conversion from NAD83 ellipsoid heights to NAVD88 orthometric heights, was downloaded from the Open Source Geospatial Foundation (2022) and used in the transformation.

Generate DEM

Bare-earth DEMs with 10-cm resolution were interpolated using the LAStools module, las2dem, from the ground classified point cloud data with noise and water removed, as pictured in Figure 20a,b. The module uses a natural neighbor interpolation algorithm implemented within las2dem. This method first creates a TIN model from the ground point cloud data. After constructing the TIN, the method rasterizes it into a regular grid to create a rasterized DEM at a specified grid cell spacing or resolution, where each cell in the grid corresponds to a height or elevation value (Z). To estimate the elevation value at each grid cell center's XY location, the algorithm uses the surrounding known data points within the TIN. It assigns weights to these points based on their relative proximity and proportionate area of influence surrounding each point. Closer points have greater weight, resulting in a smooth and natural interpolation of elevation values across the grid (Ledoux and Gold, 2005).

The ground point density for the noise and ground classified and water removed surveys were 4748 and 3845 ppm² for the 26 July and 22 September surveys, respectively. Using Equation 4, a 10 cm resolution for both surveys assured that ample coverage of the beach was provided. After, the RMSE was computed for the DEMs using the topographic RTK points from the transects, the results of which can be viewed in Table 5.

A DEM of difference (DoD) was computed using the DEMs, and the propagated uncertainty was calculated using the method shown in Wheaton *et al.* (2010), where it is defined as follows:

$$Uncertainty_{DoD} = \sqrt{(RMSE_{DEM1})^2 + (RMSE_{DEM2})^2}$$
 (6)

Using the DEM RMSE values shown in Table 5, the vertical change detection error computed to ± 0.053 m, which was

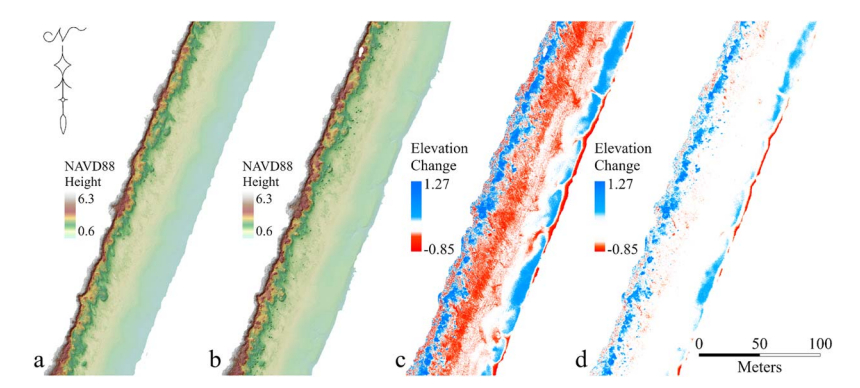


Figure 20. 10-cm DEMs of data collected of Malaquite beach on (a) 26 July 2022 and (b) 22 September 2022, (c) the computed DoD thresholded at 1σ , and (d) the computed DoD thresholded at a 95% confidence interval.

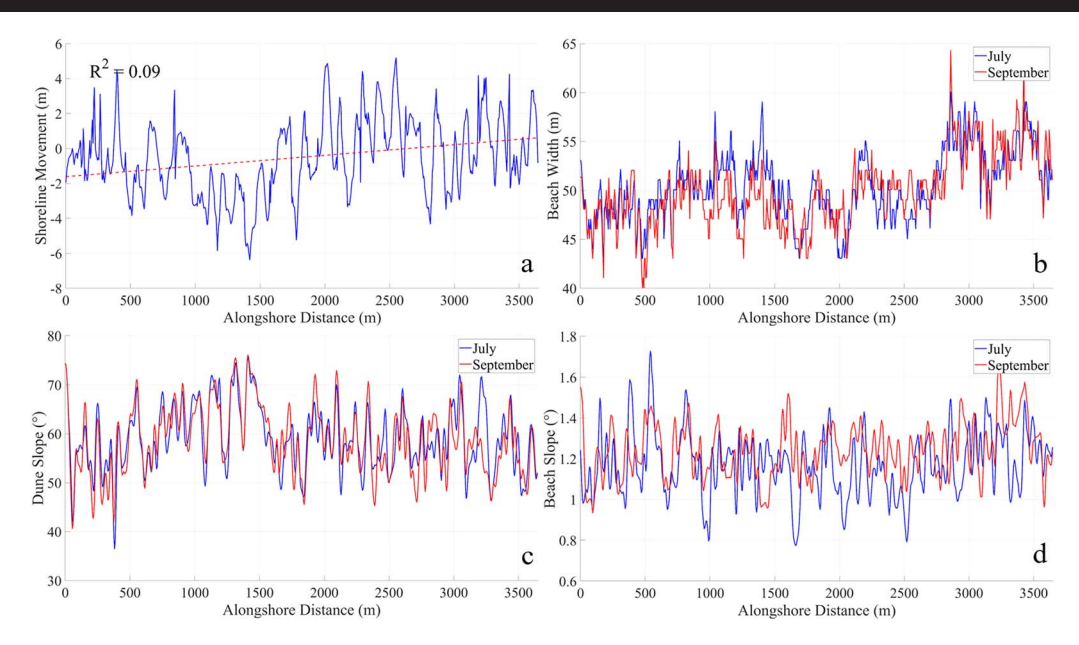


Figure 21. Alongshore plots of (a) Shoreline movement, (b) Beach width, (c) Dune slope, and (d) Beach slope from 26 July 2022 to 22 September 2022.

also the 1σ uncertainty of 68%. This value was multiplied by 1.96 to compute the 95% confidence interval, which computed to ± 0.11 m. Both confidence intervals were then applied as thresholds to the DoD, shown in Figure 20c,d, to accurately display the uncertain areas of elevation change.

It is important to note that the two surveys did not cover the same spatial extent on the shoreward side of the study site. Between July and September, the shoreline shifted further shoreward, resulting in areas that were present in one DEM but absent in the other. These regions were assigned null values in the DoD calculation. Additionally, this method assumes a uniform uncertainty across the entire dataset, meaning spatial variations in error are not explicitly accounted for. Uncertainty in DEMs is often spatially variable and influenced by factors such as surface roughness, vegetation, distance from the scanner, data acquisition conditions, etc. Error also tends to increase in areas of dense vegetation. Lidar returns from vegetation often exhibit greater vertical variability, leading to higher DEM errors. Within the dune environment, vegetation density can obscure the ground surface, causing reduced accuracy in elevation change detection.

Feature Extraction

Feature extraction was conducted in ArcGIS Pro to compute shoreline movement, beach width and slope (from the subaerial beach to the dune toe), and dune slope (from the dune toe to the top of the first shoreward facing dune in some areas), alongshore based on cross-shore profiles. The dune toe was delineated using shaded relief and the surveyed topographic transects, which were collected from the wet/dry line to the dune toe. The shoreline was delineated using an adapted MHW elevation proxy. MHW at the survey location was 0.314 m NAVD88, which was not captured in either survey. To address this issue, 10 cm was

added to the MHW elevation proxy until a contour fit both models, resulting in an elevation of 0.514 m NAVD88. An alongshore baseline was digitized using a shoreline buffer. Perpendicular 200-m-long cross-shore transects were generated every 5 m in the alongshore direction. Elevation values from the DEMs were extracted every 1 m along the transects, and the ET GeoWizards toolbox extension (ET Spatial-Techniques, Faerie Glen, South Africa) was used to compute beach width, beach slope, and dune slope for each profile, as pictured in Figure 21 (Culver et al., 2020). The slope of each transect was calculated by first finding the slope of each 1 m segment of the polyline with:

$$Slope_n = \tan^{-1} \left(\frac{\sum \Delta z_n}{\sum length_n} \right)$$
 (7)

where, Δz_n is the difference of z values of the start point and endpoint of each segment in a polyline, denoted by $\Delta z_n = |z_a - z_b|$, where z_a is the start point of the segment and z_b is the endpoint of the segment. Then, the slope of each respective segment was averaged to find the slope of the transect with $Slope_t = \sum Slope_n$. Matlab (MathWorks, Natick, Massachusetts) was then used to compute and plot shoreline change (Figure 21a). The beach width, beach slope, and dune slope were computed, along with the standard deviation, as shown in Table 6.

Results

The feature extraction results revealed that the shoreline moved up to 6 m in some areas (Figure 21a), which highlighted the seasonal dynamics and variability of this beach. The beach width changed but stayed similar in most areas alongshore, as seen by the average values in Table 6 and pictured in Figure 21b. The beach slope was variable in some

Table 6. Average value and standard deviation of beach width, beach slope, and dune slope.

| | Average | | Standard Deviation | |
|-----------------|-----------------|----------------------|--------------------|----------------------|
| | 26 July 2022 | 22 September 2022 | 26 July 2022 | 22 September 2022 |
| Beach width (m) | 59.08 | 58.75 | 6.55 | 6.89 |
| Beach slope (°) | 1.17 | 1.23 | 0.15 | 0.13 |
| Dune slope (°) | 50.35 | 49.87 | 3.48 | 3.60 |

areas, likely due to the shoreline shift, but averaged less than 1.5°, as seen in Table 6 and pictured in Figure 21d. The berm was more pronounced in September, with a steeper slope than in July, which likely explains the difference in beach slope as seen in Figure 21d and likely explaining the shoreline variability seen in Figure 21a. The dune slope also changed little alongshore, varying less than 0.5°, indicating that the dunes were stable throughout the season, as pictured in Figure 21c. It was noted that the lidar coverage of the dunes was inconsistent, with some areas capturing up to the top of the front face of the dune, while others were limited in elevation. This was likely due to the vehicle-mounted nature of the system, which may have been unable to capture the higher portions of the dunes. Additionally, occlusion from dense vegetation likely contributed to gaps in the point cloud coverage, particularly in areas with thick dune vegetation.

The DoDs pictured in Figure 20c,d display over to 1 m of accretion in the dunes, which was likely due to vegetation growth and inconsistencies in ground filtering. They also picture erosion of almost 1 m near the shoreline, which was likely caused by shoreline retreat and a more pronounced berm later in the season. Otherwise, the elevation change on the flat beach was very low. The masked uncertainty was applied primarily to the flat portion of the beach, from the approximate berm to the approximate line of vegetation, particularly in the 95% confidence interval thresholded DoD. This stresses the importance of the individual and

cumulative vertical errors in any MLS survey and their influence on resulting models and analyses.

DISCUSSION AND RECOMMENDATIONS

This workflow offers guidelines and steps to assess a mapping-grade MLS system for use in sandy beach environments, plan and conduct coastal corridor surveys, and postprocess the data to generate a DEM product, ready for coastal analyses. This section discusses key takeaways and recommendations for developing and applying this workflow, or parts of this workflow, to other systems.

Sensor Characterization and Setup

After the system was unboxed and all pieces were accounted for, it was critical to perform preliminary surveys, assuring that the system was stably mounted and collecting data correctly. In this study, it was discovered that mounting on the roof of a UTV produced too much vibration, so rubber dampeners were adapted to reduce it. It was also found that the lever arm was not rigid and was reinforced with extra metal plates. In addition, the suction cups made for mounting on the roof of a vehicle lost suction on rough terrain, so ratchet straps were used to stabilize the frame and assure a safeguard for the system. As with any system, preliminary tests were needed, and the system was adapted according to the user's needs.

Lever arm measurements and LIDAR boresight calibration validation were essential procedures in this study, because they were necessary to produce useable point cloud data. If a system is purchased with everything integrated, the manufacturer typically performs calibration procedures and provides the values with the system, and it is recommended to validate them before conducting surveys. It is also recommended to remeasure lever arm offsets and boresight angles periodically as part of routine maintenance (Olsen *et al.*, 2013), when visible misalignments in overlapping passes occur, or when a sensor has been moved or reinstalled. The methods described in this study are but one of many ways to perform these procedures. Li, Tan, and Liu, 2019, used an

Table 7. Software and websites used in the case study.

| Phase | Software | Purpose |
|-------|-------------------------------------|---|
| 1 | Terrasolid | Lidar boresight calibration |
| 1 | LadybugCap Pro | Camera boresight calibration |
| 1 | QT Modeler | Camera boresight calibration, clip point clouds for ranging error characterization |
| 1 | CloudCompare | Ranging error characterization computation |
| 2 | Weather sites and apps | Beach conditions (wind strength and direction, wave height and direction, temperature, and cloud cover) |
| 2 | NOAA's tide and current predictions | Beach conditions: check time of low tide and height |
| 2 | NOAA's inundation dashboard | Beach conditions: inundation predictions |
| 2 | GNSS Mission Planning | GNSS conditions: satellite position and coverage |
| 3 | Inertial Explorer | Trajectory processing and analyses |
| 3 | ScanLook PC | Point cloud processing |
| 3 | Ladybug Export | Point cloud colorization |
| 3 | Spatial Explorer | Strip adjustment validation and apply control points |
| 3 | LAStools module lascontrol | Vertical error quantification |
| 4 | LAStools module lasnoise | Noise removal |
| 4 | LAStools module lasground | Ground-point classification |
| 4 | QT Modeler | Water-point classification |
| 4 | LAStools module lasvdatum | Vertical datum conversion |
| 4 | LAStools module las2dem | Generate DEM |

Iterative Closest Point (ICP) algorithm with certain settings to align overlapping strips and compute misalignments between points collected in different strips and directions as a method of boresight calibration. Yu et al. (2021) performed boresight calibration and lever arm offset measurements using both planar and spherical features. Instead of matching only planar features, spherical features were also included, and a Random Sample Consensus algorithm was used to automatically extract and match corresponding features to compute extrinsic calibration parameters. Additional calibration beyond boresight in this study can also be completed to calibrate every laser in a multi-laser system. Hurst (2014) calibrated every laser in a Velodyne HDL-32E, thus improving the final point cloud, which could be implemented in future work.

Determining the optimal effective range for the lidar sensor was crucial to minimize ranging error, plan for multiple passes, and decrease point cloud variability (Schaer et al., 2007). Preliminary point cloud data showed noise at extended ranges, emphasizing the need for a distance filter. Through the controlled experiment executed in this study, which was conducted against a vertical wall in a parking lot, an optimal range of 70 m was determined, which aligned with the findings from Chan, Lichti, and Belton (2013) for the Velodyne HDL-32E used in this study. However, this test environment differed from the beach conditions that this study is tailored to. Factors such as reflective dry sand, absorptive wet sand, dense dune vegetation, and complex topography (e.g., sloped dunes) can all influence the effective range of a LIDAR system by affecting return strength, incidence angle, and measurement precision.

In coastal environments, especially wide beaches with tall dunes and densely vegetated foredunes, reducing the maximum scanning range to minimize errors should be balanced against the need to capture distant terrain features. While a shorter range helps reduce beam spread and ranging error, it risks missing some topographic elements. This should be considered when choosing an effective range for a given system and one can be conservative or increase the effective range if farther features are targeted. Multiple passes are often needed to mitigate shorter ranges and ensure full coverage of the beach, shoreline, and foredune.

Although the experimental setup was not conducted on the beach, the goal was to isolate range-induced variability in a controlled, static environment. It is possible that repeating the same experiment on a sandy beach could yield a different optimal range. This workflow provided an example of how to characterize an optimal effective range of a LIDAR system and provides a framework for applying those findings in a step-by-step methodology.

Additionally, coastal surveys often require multiple passes to compensate for data occlusion caused by the vehicle, objects on the beach, behind the berm, *etc.* In such cases, post-processing techniques like strip adjustment are necessary to align overlapping scan lines and improve data fidelity (Bitenc *et al.*, 2011; Nahon *et al.*, 2019; Wang *et al.*, 2018). Therefore, it is essential to tailor the experimental design and scanning strategies to the specific LIDAR system and environmental conditions of each survey location.

In the future, the authors would like to apply the algorithms presented in Kelly *et al.* (2022), who evaluated a Velodyne HDL-32E's ranging performance to scanner internal temperature. They found a positive correlation between effective range and internal temperature, recommending the scanner be operated for 30 minutes before surveying. They also found that conducting a survey at night reduced the RMSE by up to 5%. In addition, to mitigate the scanner temperature or ranging error, the linear regression models presented in their study decreased the RMSE by approximately 88%. This could potentially help increase data fidelity, particularly in very hot or cold coastal areas/times of year.

Quality Assurance

An INS initialization experiment determined an optimal initialization procedure for the mapping-grade MLS system used in this study. According to Niu et al. (2015), the initial velocity error of an IMU determines the drift and attitude errors later in a survey. The INS initialization procedure in this study decreased the vertical error of the surveys and oriented the INS using kinematic alignment procedures before the LIDAR system began collecting. Without proper initialization, the vertical error was high at the beginning and end of the surveys, with the initial error determining the accuracy of the final trajectory. Therefore, minimizing INS errors before a survey was crucial for obtaining more accurate trajectory information. It is also important to note that the kinematic procedure was repeated in reverse after a survey to enable comparison of forward and backward processed trajectories, perform tightly coupled combined forward and backward processing, and assess forward-backward offsets to smooth and generate a best estimated trajectory.

It was also observed that a system could be initialized offsite if there was not enough space on the beach. This could mean initializing in a parking lot and driving to the study area before collecting LIDAR data. However, the need for an INS initialization procedure may depend on the type and quality of the IMU that is used. Higher end IMUs can increase the accuracy of an INS but can significantly increase the cost of a system (Niu *et al.*, 2015). However, many mapping-grade systems integrate MEMS-IMUs, which introduce more errors. The MEMS-IMU initialization experiment presented in this study provides an example of how to determine whether a complex driving procedure is necessary (NovAtel, 2013). Therefore, one should check system specifications and, if unsure, an INS initialization experiment can help to make this determination.

To ensure each survey was conducted effectively and under optimal conditions, specific parameters and environmental circumstances were planned in advance. These included metocean conditions, weather conditions, and local driving factors. This preparation helped to optimize the process and targeted ideal conditions. Driving speed and maneuvers were kept in accordance with local laws and regulations. However, a speed that accounts for scanner pulse rate, length of survey, and vibration effects should be considered to achieve the desired point density.

Puente *et al.* (2013) developed an equation to compute point density, in ppm², of MLS systems based on the scanner pulse rate, scan speed, vehicle driving speed, and distance from the

lidar scanner. However, it's important to note that MLS systems scan radially, meaning the point density increases closer to the lidar scanner (Ma et al., 2018). In this study, a speed limit of 6.4 m/s was enforced on the study beaches. However, a maximum driving speed of 4.5 m/s provided a point cloud density of over 200 ppm² per pass and over 400 ppm² for two passes (in single return mode) using the MLS system in this study. This also accounted for rough terrain and reduced vibration, particularly in the back beach. This parameter was determined from initial surveys and in the case of rough terrain or a crowded beach, this speed was reduced, resulting in higher point densities. Occlusion was also a key consideration during the surveys. When the beach was crowded with beach tents, umbrellas, vehicles, and people, it occasionally became necessary to drive in front of beachgoers to minimize data gaps and ensure sufficient coverage. Scan lines also took place close to the berm and incipient dunes to reduce occlusion.

Favorable weather and low-tide conditions were difficult to achieve, particularly during seasons with high wave runup. Sometimes, the best conditions possible were targeted. One such instance occurred when planning a survey in February 2023. Although the crew aimed to conduct the survey at low tide, strong onshore winds rendered sections of the beach impassable. Instead, they adjusted by targeting offshore or cross-shore winds. These ideal conditions never aligned simultaneously that month, forcing the crew to prioritize which factor was more favorable for the survey.

LIDAR can also be operated effectively in darkness, allowing for surveys to be collected after sundown. This capability is particularly advantageous for avoiding unfavorable daytime weather conditions and crowded beaches. However, if imagery is also being collected, it is preferrable to conduct surveys during daylight hours with optimal lighting conditions to ensure high-quality data.

Lastly, some beaches may not have enough driving space to complete two passes, particularly at times of year with high wave runup. Al-Rawabdeh *et al.* (2020) used MLS to monitor transportation corridors to assess the structural integrity of mechanically stabilized earth walls. Because only one pass could be completed, they recommended two LIDAR scanners for the single pass to increase coverage and point density.

In this study, a local, centralized base station was occupied on an assumed coordinate and adjusted after each survey for performing PPK GNSS trajectory corrections. As a result, every survey contained unique base station coordinate uncertainty, propagating into the trajectory solutions and contributing to the final product's cumulative uncertainty. This approach was chosen to enable the base station to support local RTK topographic data collection for quality control of the MLS surveys. The uncertainty in the assumed base station coordinate primarily impacts repeat MLS surveys for elevation change detection. Ideally, occupying a known, stable coordinate or benchmark would eliminate this error across multiple surveys by providing a consistent reference point. This approach aligns with the goals of this study to minimize vertical error. However, because of a lack of stable benchmarks in the vicinity with sufficient coverage to perform RTK, the option was not viable. For future repeat surveys, using a consistent, known coordinate or benchmark is recommended (CALTRANS, 2018; Olsen *et al.*, 2013).

Data Processing and Quality Control

Determining the more accurate method of inertial navigation (GNSS+INS) trajectory processing and the need for strip adjustment was essential to minimize vertical error. By addressing each step of processing, the workflow effectively reduced variability, enhanced alignment of multiple passes, and ensured consistency across multiple datasets.

Trajectory Processing determined that tightly coupled processing generally achieved higher accuracy than loosely coupled processing. This was likely because the surveys were linear with little to no turning. This caused IMU drift due to lack of dynamic driving, as evidenced by Falco, Pini, and Marucco (2017). In later projects, tightly coupling produced trajectories with consistently higher accuracies, validating the findings of the trajectory processing experiment. As mentioned earlier in this paper, tightly coupled architecture generally performs better, particularly in areas of poor GNSS coverage as explained in Tang et al. (2023) and stated in Pöppl et al. (2023). In loosely coupled, the processed trajectory does not have a position for the time of GNSS signal loss, whereas tightly coupled does compute a partial adjustment for the lack of GNSS coverage (Boguspayev et al., 2023). Therefore, tightly coupled processing is generally recommended. However, it is advised that initial surveys be processed using both loosely and tightly coupled methodologies to determine which provides more accurate data for a specific system and project needs (Falco, Pini, and Marucco, 2017). Also, repeating an INS initialization procedure at the beginning and end of each survey will allow these experiments to be performed. Plotting the trajectory accuracy, forward and reverse processing plots, and others can be a useful tool to determine how well each method works.

After colorizing the point cloud, high elevations still included a great number of falsely colorized points. Upon further evaluation, the camera and lidar timing were not synchronized and the tools being used were not efficient to adjust the camera parameters and provide the desired outcome. In the future, the authors will streamline the data processing procedures in one software which has the capability to geolocate, strip adjust and colorize the point cloud. During point cloud colorization, the software will have the capability to adjust the camera boresighting and timing errors by picking corresponding points/features in the point cloud and imagery. Additionally, González et al. (2022) explained that colorization errors can be due to differing resolutions between the camera and LIDAR scanner, boresighting errors, timing errors, and camera perspective. The camera resolution may cause the assignment of more than one pixel per lidar point and features on the horizon are often assigned the color of the sky. They adjusted their point clouds by identifying sky-colored points and replacing the color with that of neighboring points. There are other methods to improve colorization including image masking and the method outlined in Xu et al. (2023), where a Gaussian distribution-based colorization method was adopted. They also implemented a central area cutoff to reduce colorization errors from image edges. Additionally, Liu *et al.*, 2024 used a novel algorithm called OmniColor to improve colorization with a spherical camera, while taking advantage of the wide view of each image frame and minimizing spherical distortion. The methods use a camera frame of reference, eliminating LIDAR points that are outside of the image frame.

Strip adjustment is a critical step in most MLS system workflows, serving to improve the internal geometric consistency of overlapping scan lines. While this process can enhance absolute accuracy, particularly when used in combination with GCPs, its primary purpose is to refine the relative alignment of overlapping strips. In this study, while overlapping passes appeared to be well-aligned, noticeable misalignments were present near the edges of the scan lines, particularly in the complex dune system. This highlights that even with good initial calibration and direct georeferencing, strip adjustment is often required to correct subtle trajectory and orientation errors that accumulate over time or vary by surface type or distance from the scanner. Evaluating the success of a strip adjustment should include not only RMSE comparisons to GCPs, but also through internal precision metrics that quantify how well strips align. These are usually available through post-proccing reports. If a system is well calibrated and multiple passes are well aligned, the adjustment may only be minor. However, many lower-grade systems generally have a poorer-quality trajectory and resulting point cloud than those of survey-grade systems. This will likely result in more adjustments when strip adjustment is performed and should be performed as a best practice, as outlined in Baraja (2021), Huntington and Williams (2024), and Olsen et al. (2013). While internal precision reports were not available for this study, future work will incorporate tools that generate these metrics to better assess the effects of strip adjustments.

The GCP experiment presented in this study illustrated a method for evaluating and selecting an optimal GCP configuration tailored for a specific user's needs, equipment, or beach environment. The configuration and spacing chosen were well suited for smaller projects less than approximately 8 km. However, for larger projects, adjustments would be required. This limitation should be determined by the users and will likely vary by several factors including manpower, vehicles, targets available, and baseline length and range for RTK, amongst other things. The experiment also highlighted the importance of evaluating GCP application thoroughly, because outliers could affect point cloud accuracy. In this case, targeted checkpoints were viable GCP replacements and could help to eliminate blunders from the control setup, reducing the error of the final dataset. As mentioned above, GCPs in this study were applied during strip adjustment to correct trajectory drift, improve vertical accuracy, and resolve misalignments between overlapping scan lines. GCPs may also be applied to adjust horizontal accuracy, which was not discussed in this study.

The ASPRS's Positional Accuracy Standards, edition 1, were used as a guideline in this study. However, after this study took place the ASPRS Positional Accuracy Standards, edition 2 were published. The edition 1 standards provided guidelines to plan surveys and assess accuracy in both

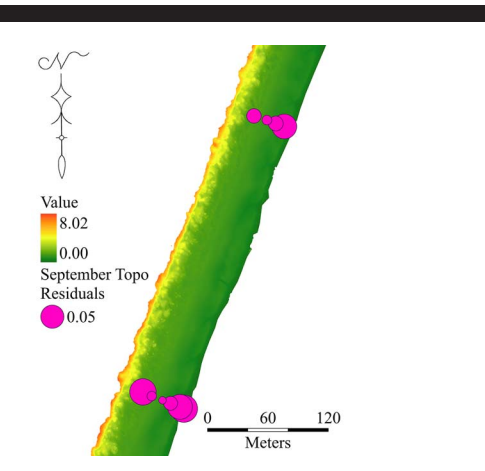


Figure 22. Visualization of the difference between DEM and corresponding topographic points of the 22 September 2022 survey, demonstrating that topographic checkpoints provide good representation of vertical error—especially radially from the scanner path, where the error increases.

vegetated and unvegetated terrain. The standards stated that a minimum of 20, (ideally 30) evenly spaced checkpoints should be collected (ASPRS, 2004). It is a best practice to adhere to a set of accuracy standards to ensure data quality and integrity. While the authors used the ASPRS Accuracy Standards, other standards may be adhered to.

Targeted and topographic checkpoints served as independent datasets used for assessing vertical accuracy of the point clouds and DEM products and played a very important role, as they were used to assess the vertical accuracy of the surveys. The targeted checkpoints did not represent the range of terrain of the beach environment. However, the topographic checkpoints, collected from the shoreline to the dune toe, encompassed a diverse range of terrain and provided a better measure of vertical accuracy. This is illustrated by Figure 22, which is an example of a topographic checkpoint dataset, demonstrating that topographic points farther from the system path exhibited greater discrepancies from the DEM. According to ASPRS (2024), checkpoints should be placed away from GCPs, to reduce vertical error bias in accuracy assessments, but in an area that will not be prone to interpolation errors in the final product. Targeted checkpoints can also be used to compute the horizontal and vertical accuracy of a survey. These should be located using intensity, instead of color (if using a colorized point cloud). This is due to the possibility that colorization did not align well with the point cloud.

The targets used in this study were handmade from plywood and later replaced by custom commercially printed polyvinyl chloride (PVC) targets. Many GCP materials, patterns, and configurations were available for purchase. The material options included vinyl, plastic, aluminum, and cardboard. Patterns included dot, cross, and checkerboard. The aforementioned materials were deemed too fragile, would rust quickly, or could easily be moved by wind, animals, or people. Unexpected wave runup could also displace or disintegrate them. Heat and sun exposure were highly considered.

In south Texas, the heat index rises well above 37°C, and prolonged sunshine could warp and bend certain materials. Because of these factors, it was found that the plywood or PVC were sturdier than the other materials. The plywood targets were hand-painted black, with a white cross pattern on one side and a dot on the other. The white paint was mixed with reflective glass powder to increase the albedo, and a reflective, adhesive survey target was affixed to the center of each circle on the side with the dot. However, these targets bowed in severe heat. They were later replaced by custom commercially printed PVC targets, which were more rigid when exposed to severe conditions. However, they also bowed in severe heat, but not as much as the plywood.

Selection of GCP material, pattern, and configuration may vary based on the beach environment, MLS system, and processing software. It's recommended that commercially available targets be thoroughly considered before purchase. Static features can also serve as GCPs but are not often available in dynamic sandy beach settings. In addition, clear warnings for beachgoers are advised. Using wooden stakes with survey flagging or painting "survey target, do not move" on the target itself proved effective in discouraging tampering. Without these markers, targets were sometimes disturbed by pedestrians or vehicles.

Postprocessing

Postprocessing required trial and error to identify appropriate filtering settings and preferred methods of vertical datum conversion and DEM generation. This section discusses the lessons learned in postprocessing procedures.

Different point cloud filtering and classification software that were available to the authors were tested and evaluated in development of the workflow. To classify noise the authors evaluated the use of a moving window to isolate point clusters of a specified density and a gridded filter of a specified size to isolate point clusters of a specified density. The gridded filter of a specified size was deemed effective at removing noise caused by flocks of birds flying overhead, erroneous data, and other random clusters of points.

To classify ground points, a revised progressive TIN densification algorithm (Nie et al., 2017), discussed earlier in this paper, was used. Experimenting with different settings was necessary to identify which were the most effective for the data collected in this study. No classification algorithm was perfect, and the point clouds were always thoroughly reviewed to ensure that unwanted points were accurately classified or removed. On survey days with many birds present on the beach, it was challenging to apply noise and ground filters successfully. The birds created dense point clusters, which were incorrectly classified as ground.

It is important to emphasize that user experience and familiarity with tuning and adjusting the parameter settings plays an important role in achieving good filtering or classification results. In cases where the algorithms didn't correctly classify points such as the bird example discussed, manual classification of points was required. Small windows/step sizes were sometimes necessary to classify small objects like vehicles, signposts, and vegetation, while larger windows/step sizes were more effective at classifying larger features

such as homes, hotels, and other structures. These steps added to the overall postprocessing time and effort.

To minimize the need for manual classification, it was beneficial to gather additional ground-truth data during surveys, such as points denoting the dune toe, vegetation line, and other natural features. Manual vetting of water removal was also required, because the reflectance of water can be similar to that of vegetation. Classification methods available to the authors were thoroughly tested before being integrated into the best-methods workflow. In the future, point cloud filtering methods for colorized point clouds will be evaluated. Accurate colorization could provide RGB values that are particularly helpful for filtering vegetation and water.

As mentioned earlier, natural neighbor interpolation was used to generate 10 cm DEMs in this study. The edges of the DEMs were closely cropped by eliminating triangles that were less than 2 m in size. Although the data was collected with occlusion in mind, generating relatively high resolution DEMs resulted in gaps in the data in these zones, which were not generated in lower resolution DEMs. This could have potentially been mitigated by using a different interpolation method. Arun (2013) compared inverse distance weighting (IDW), kriging, natural neighbor, spline, and topo to raster to generate DEMs considering various types of terrain. They found that the performance of the interpolation method varies based on the terrain. They also concluded that kriging performed better as compared with the other methods over more terrain features and topo to raster was preferred for ridge lines. Another study by Montealegre, Lamelas, and Da la Riva (2015) evaluated natural neighbor, TIN to raster, IDW, Australian national university DEM, kriging, and point to raster. They found that landcover affected the interpolations and that the TIN to raster interpolation overall produced the most accurate DEM. These studies suggest that choosing an interpolation method that is more suitable for a specific environment may further increase the accuracy of the final product. In the future, some of the interpolation methods stated here will be studied to determine which is more suitable for the sandy beach corridor environment.

The key steps presented in this study aimed to reduce the error budget as much as possible, but these errors propagated to contribute to the vertical RMSE of the final DEM product. Horizontal errors can also significantly contribute to the vertical error (ASPRS, 2004). However, in this study, the primary concern was minimizing vertical RMSE, because it pertains to beach change measurements. Because the error budget was a combination of the key steps, it is recommended that the RMSE of the final DEM be computed to assure that the postprocessing methods were satisfactory, including point cloud classification and the DEM interpolation method chosen.

Case Study: Malaquite Beach

The case study showcased the workflow in a real-world application, demonstrating the planning, execution, processing, and postprocessing stages. The final RMSE values of the two surveys were under 5 cm, which were in the range of vertical accuracy that Olsen *et al.* (2013) determined for mapping-grade systems. The case study also demonstrated some

qualitative analyses that can be computed from MLS-derived DEMs.

The DoDs showcased the elevation change of repeat surveys and demonstrated error propagation in final products. The error thresholds were based on propagated errors in the DoD based on vertical RMSE of each survey relative to the topographic checkpoints. With these repeat surveys and measurements, the DoD thresholds at 1σ and 95% confidence intervals were ± 0.05 m and ± 0.1 m, respectively. The thresholded DoD's, pictured in Figure 20c,d, demonstrated the stark difference between thresholding at lower and higher confidence intervals, showcasing that the points on the dunes and close to the shoreline were statistically significant, while the beach remained relatively stable, particularly at the 95% confidence level. However, applying the error threshold also highlighted the importance of minimizing vertical error and creating an optimized mapping-grade MLS workflow (Le Mauff et al., 2018; Wheaton et al., 2010).

The DoD indicated that the largest elevation changes occurred in the dunes and on the berm. The change in the dunes was most likely caused by vegetation incorrectly classified as ground. This was an example of imperfect MLS point cloud data and highlights the challenges associated with the oblique view and a using the LIDAR in single return mode. It was mentioned earlier that the system used in this study has a dual return mode. However, when it is turned on, the range of the LIDAR is significantly reduced. Because this effects the efficiency and ability to capture the dunes, single return mode was used. In the future, a multi-return MLS system would be beneficial to survey these environments, which could aid point cloud classification. The oblique view of the MLS system was also challenging, as the foredune crests were not captured in many places alongshore, something that the nadir view of ALS or UAS systems would provide more coverage of.

The time associated with conducting, processing, and postprocessing one of the case study surveys was approximately 4 days. Minor preparation such as gathering equipment, charging batteries, and finalizing the survey plan was required the day before the survey. On the day of the survey, time was allocated to load equipment, travel to and from the study site, and clean and unload the gear afterward. The fieldwork itself took 4 to 4.5 hours with a three-person crew. This included base station setup, laying and georeferencing targets, collecting topographic transects, performing the MLS survey, and breaking down the equipment. The most time consuming of these actions was collecting the groundtruth data and laying the ground targets. The number of ground targets limited the surveys to a maximum length of about 8 km (driving at a speed of $\sim \! 4.5$ m/s, a survey of this length would take approximately 1 hour to complete). In the case study, the actual MLS survey portion lasted around 30 minutes. An additional 2 days were dedicated to data processing and postprocessing, with the most time-consuming tasks being point cloud classification and DEM generation.

As stated in Hauser, Glennie, and Brooks (2016), survey-grade MLS systems can cost hundreds of thousands of dollars, are large, and are challenging to operate. Some are limited to a single platform, limiting their use in certain environments and

restricting them to certain areas. Yen, Ravani, and Lasky (2011) conducted a cost analysis of mapping- and survey-grade MLS systems for transportation and found that while survey-grade systems were more expensive to operate, they met a broader range of project requirements than mapping-grade systems. At the time of this study, a mapping-grade MLS system could be acquired for under \$100,000 USD, with the system in this study costing around \$75,000 USD at the time of purchase. The authors also consulted with RIEGL for typical MLS pricing. They were informed that, depending on the system configuration, training, and software, some mapping-grade systems can cost more than \$150,000 USD, while some survey-grade systems may exceed \$700,000 USD. However, MLS technology is becoming more cost-effective over time, with some systems available for as low \$40,000 USD. Importantly, many coastal corridor surveys do not require the same high precision standards of highway or construction projects. Quantifying coastal geomorphology does not typically demand millimeter level precision, which can significantly reduce both equipment costs and data delivery times.

Depending on the system and configuration, some mappinggrade systems have vertical accuracies comparable to those of survey-grade systems. Lin, Manish et al. (2021) compared a range of MLS systems for their applicability in mapping roadside ditches. In their analyses, they found that the difference between their mapping- and survey-grade system surveys were 0.018 m RMSE, 0.013 m standard deviation, and -0.012 m mean. However, the approach and manner of planning, conducting, and processing a survey can highly influence the result. As an example, Mandlburger et al. (2023) compared a mapping- and survey-grade UAS-mounted MLS system. The resulting surveys showed that the survey-grade system achieved strip misalignment of 2 cm, whereas the mapping-grade system had strip misalignment of ± 10 cm. It was deemed that the misalignment was poor because of boresight calibration error. Although this study was collected using UAS-mounted MLS systems, this is a great example of why and how the workflow presented in this study is applicable and necessary.

CONCLUSIONS

Mapping-grade MLS systems equipped on all-terrain vehicles for surveying of sandy beach corridors can provide consistent, accurate topographic point cloud data with high spatial resolution of the beach and lower foredune from a terrestrial perspective. However, despite the misconception that these systems are "plug and play," ready for data collection, they should be evaluated, performance characterized, and sources of error minimized to generate consistent, accurate point cloud data. This study evaluated a miniaturized, mapping-grade MLS system, called the HiWay Mapper, integrated with a Velodyne HDL-32E lidar sensor and developed a survey workflow for repeatable data acquisition. While the accuracy of mapping-grade MLS data cannot be fully guaranteed, the survey workflow presented in this study offers a systematic framework designed to help ensure the repeatability of beach elevation measurements for monitoring sandy beach corridors using MLS systems. The workflow is presented in four phases: (1) sensor characterization and setup, (2) quality assurance, (3) data processing and QC, and (4)

postprocessing. The cumulative implementation of the key steps outlined and tested in this study were essential for enhancing the vertical accuracy of the point cloud data and using the data to generate the final survey product, a bare-earth DEM of the sub-aerial beach and lower foredune system. Each stage is an important component in contributing to the overall quality and reliability of the MLS-derived DEM product.

In this study, lever arms were manually measured, LIDAR and camera boresight calibration validation was conducted, and ranging error characterization took place. The lever arm measurement revealed that hand measurements were significantly different from the given values. The LIDAR boresight calibration validation also provided sizable corrections to the existing values. These together considerably decreased point cloud noise while increasing visibility and alignment. Camera boresight calibration validation verified the existing values and assured repeatability. Lastly, ranging error characterization evaluated the effective range of the LIDAR scanner to reduce range-induced noise.

An initialization experiment was conducted which evaluated five initialization procedures varying in complexity, revealing the need for dynamic driving immediately before and after each survey. Trajectory processing evaluated loosely and tightly coupled processing methods and determined that tightly coupled methodology generally achieved higher vertical accuracy. Strip adjustment validation compared point cloud results with and without strip adjustment, finding that strip adjustment increased the vertical RMSE and aligned points farther away from the MLS system, particularly in the dunes. A control layout and checkpoint experiment evaluated the vertical RMSE of five GCP configurations at six varying intervals and their effect on increasing the vertical accuracy, finding a pattern and spacing that was suitable for adjusting each survey without expending too many targets and taking too much time from a survey.

The case study on Malaquite beach at PAIS demonstrated the use of the optimized survey workflow. Two surveys were conducted in July 2022 and September 2022 to study seasonal variability of sea turtle nesting habitats. The DEMs achieved vertical RMSEs of 0.039 and 0.037 m, respectively. The DEMs were then used to extract shoreline movement, beach width, beach slope, and dune slope using cross-shore transects. These revealed significant beach geomorphology changes during the nesting season, including shoreline change of up to 6 m, prompting changes in beach width and slope. A DoD with a 1σ uncertainty of ± 0.05 m and 95% confidence interval of ± 0.1 m showed an elevation change of up to 0.9 m. The uncertainty masks also emphasized the importance of vertical uncertainty and its effect on resulting statistical significance on resulting products and measurements.

ACKNOWLEDGMENTS

This publication was supported in part by federal funds under award NA18NOS4000198 from NOAA, U.S. Department of Commerce and in part by the National Science Foundation (NSF) CREST-GEIMS Center under Award 2112631. The statements, findings, conclusions, and recommendations are those of the author(s) and do not necessarily reflect the views of NOAA, the U.S. Department of Commerce, and NSF.

LITERATURE CITED

- Abdulrahman, F.H., 2013. The Use of Targets to Improve the Precision of Mobile Laser Scanning. Nottingham, United Kingdom: University of Nottingham, Ph.D. dissertation, 346p.
- AccuWeather, Inc., 2025. Current Conditions. (Accessed September 22, 2022). AccuWeather [Mobile App]. https://www.accuweather.com/
- Aevex Aerospace, 2024. LIDAR sensors, simplified: Part 2—LIDAR systems range and architecture. https://geodetics.com/lidar-sensors-simplified-part-2/
- Al-Rawabdeh, A.; Aldosari, M.; Bullock, D., and Habib, A., 2020. Mobile LIDAR for scalable monitoring of mechanically stabilized earth walls with smooth panels. Applied Sciences, 10(13), 4480. doi:10.3390/app10134480
- Alsadik, B., 2024. Performance assessment of mobile laser scanning systems using velodyne hdl-32e. *Journal of Civil Engineering Frontiers*, 5(1), 7–12. doi:10.38094/jocef50177
- Arun, P.V., 2013. A comparative analysis of different DEM interpolation methods. *Geodesy and Cartography*, 39(4), 171–177. doi:10. 3846/20296991.2013.859821
- ASPRS (American Society of Photogrammetry and Remote Sensing), 2004. ASPRS guidelines; Vertical accuracy reporting for LIDAR data. Edition 1. https://www.asprs.org/a/society/committees/lidar/Downloads/Vertical_Accuracy_Reporting_for_Lidar_Data.pdf
- ASPRS (American Society of Photogrammetry and Remote Sensing), 2024. ASPRS Positional Accuracy Standards for Digital Geospatial Data. Edition 2, Version 2. https://asprsorg.sharepoint.com/sites/PublicAccess/Shared%20Documents/Forms/AllItems.aspx?id=%2Fsites%2FPublicAccess%2FShared%20Documents%2FPublic%5FDocuments%2FStandards%2F2024%5FASPRS%5FPositional%5FAccuracy%5FStandards%5FEdition2%5FVersion2%2E0%2Epdf&parent=%2Fsites%2FPublicAccess%2FShared%20Documents%2FPublic%5FDocuments%2FStandards&p=true&ga=1
- Bailey, G.; Li, Y.; McKinney, N.; Yoder, D.; Wright, W., and Herrero, H., 2022. Comparison of ground point filtering algorithms for high-density point clouds collected by terrestrial LIDAR. Remote Sensing, 14(19), 4776. doi:10.3390/rs14194776
- Baraja, 2021. Effective range and why it matters more than maximum range. https://www.baraja.com/en/blog/effective-range-matters-more-than-maximum-range
- Barber, D.M. and Mills, J.P., 2007. Vehicle based waveform laser scanning in a coastal environment. *Proceedings of 5th International Symposium on Mobile Mapping Technology* (Padua, Italy), p. 6.
- Bitene, M.; Lindenbergh, R.; Khoshelham, K., and Van Waarden, A.P., 2011. Evaluation of a LIDAR land-based mobile mapping system for monitoring sandy coasts. *Remote Sensing*, 3, 1472–1491. doi:10. 3390/rs3071472
- Boguspayev, N.; Akhmedov, D.; Raskaliyev, A.; Kim, A., and Sukhenko, A., 2023. A Comprehensive Review of GNSS/INS Integration Techniques for Land and Air Vehicle Applications. Applied Sciences, 13(8), 4819. doi:10.3390/app13084819
- Bracewell, J., 2023. Coastal dynamics monitoring at Padre Island National Seashore, Texas: 2017–2023. https://www.nps.gov/articles/ 000/guln_coastal-dynamics-monitoring-pais-2023.htm
- Brooks, B.A.; Glennie, C.; Hudnut, K.W.; Ericksen, T., and Hauser, D., 2013. Mobile laser scanning applied to the earth sciences. *EOS*, 94(36), 313–315. doi:10.1002/2013EO360002C
- Brzank, A. and Heipke, C., 2012. Classification of LIDAR data into water and land points in coastal areas. *International Archives of Photogrammetry and Remote Sensing*, 36, 1–6. https://www.isprs. org/proceedings/xxxvi/part3/singlepapers/P_19.pdf
- CALTRANS (California Department of Transportation), 2018. CALTRANS surveys manual: 15—Terrestrial laser scanning specifications. https://dot.ca.gov/programs/right-of-way/surveysmanual-and-interim-guidelines
- Chan, T.O.; Lichti, D.D., and Belton, D., 2013. Temporal analysis and automatic calibration of the Velodyne HDL-32E LIDAR system. ISPRS Annals of Photogrammetry, Remote Sensing and Spatial Information Sciences, II-5/W2, 61–66. doi:10.5194/isprsannals-II-5-W2-61-2013

- Chen, J.; Wang, H., and Yang, S., 2023. Tightly coupled LIDAR-inertial odometry and mapping for underground environments. Sensors, 23, 6834. doi:10.3390/s23156834
- Chen, Z.; Li, J., and Yang, B., 2021. A strip adjustment method of UAV-borne LIDAR point cloud based on DEM features for mountainous area. *Sensors*, 21, 2782. doi:10.3390/s21082782
- CloudCompare, 2023. CloudCompare version 2.6.1: User manual. https://www.cloudcompare.org/doc/qCC/CloudCompare%20v2.6.1% 20-%20User%20manual.pdf
- Cooper, R.J.; Sundin, G.; Čederbaum, S.B., and Gannon, J.J., 2005. Natural resource summary for Padre Island National Seashore (PAIS). Final report to National Park Service Gulf Coast Network. https://irma.nps.gov/DataStore/Reference/Profile/590835
- Culver, M.; Gibeaut, J.C.; Shaver, D.J.; Tissot, P., and Starek, M., 2020. Using Lidar data to assess the relationship between beach geomorphology and Kemp's ridley (*Lepidochelys kempii*) nest site selection along Padre Island, TX, United States. Frontiers in Marine Science, 7, 214. doi:10.3389/fmars.2020.00214
- Elhashash, M.; Albanwan, H., and Qin, R., 2022. A review of mobile mapping systems: From sensors to applications. *Sensors*, 22(11), 4262. doi:10.3390/s22114262
- Falco, G.; Pini, M., and Marucco, G., 2017. Loose and tight GNSS/INS integrations: Comparison of performance assessed in real urban scenarios. Sensors, 17(2), 255. doi:10.3390/s17020255
- Gillins, D.T.; Kerr, D., and Weaver, B., 2019. Evaluation of the Online Positioning User Service for processing static GPS surveys: OPU-S-Projects, OPUS-S, OPUS-Net, and OPUS-RS. *Journal of Survey*ing Engineering, 145(3), 05019002. doi:10.1061/(ASCE)SU.1943-5428.0000280
- Glawe, E., 2016. Demystifying mobile mapping. https://www.xyht.com/lidarimaging/demystifying-mobile-mapping/
- Gong, J.; Li, Z.; Zhu, Q.; Sui, H., and Zhou, Y., 2000. Effects of various factors on the accuracy of DEMs: an intensive experimental investigation. *Photogrammetric Engineering & Remote Sensing*, 66(9), 1113–1117.
- Gong, J., 2013. Mobile LIDAR data collection and analysis for post-Sandy disaster recovery. Presented at the ASCE International Workshop on Computing in Civil Engineering, American Society of Civil Engineers (Los Angeles, California), pp. 677–684. doi:10. 1061/9780784413029.085
- González, E.; Balado, J.; Arias, P., and Lorenzo, H., 2022. Realistic correction of sky-coloured points in mobile laser scanning point clouds. Optics & Laser Technology, 149, 107807. doi:10.1016/j. optlastec.2021.107807
- Guan, H.; Li, J.; Cao, S., and Yu, Y., 2016. Use of mobile LIDAR in road information inventory: A review. *International Journal of Image and Data Fusion*, 7, 219–242. doi:10.1080/19479832.2016. 1188860
- Hauser, D.; Glennie, C., and Brooks, B., 2016. Calibration and accuracy analysis of a low-cost mapping-grade mobile laser scanning system. *Journal of Surveying Engineering*, 142(4), 04016011. doi: 10.1061/(ASCE)SU.1943-5428.0000178
- Holopainen, M.; Kankare, V.; Vastaranta, M.; Liang, X.; Lin, Y.; Vaaja, M.; Yu, X.; Hyyppä, J.; Hyyppä, H.; Kaartinen, H.; Kukko, A.; Tanhuanpää, T., and Alho, P., 2013. Tree mapping using airborne, terrestrial and mobile laser scanning: A case study in a heterogeneous urban forest. Urban Forestry & Urban Greening, 12, 546–553. doi:10.1016/j.ufug.2013.06.002
- Hu, Y., 2003. Automated Extraction of Digital Terrain Models, Roads and Buildings Using Airborne Lidar Data. Calgary, Alberta: University of Calgary, Ph.D. dissertation, 200p.
- Huntington, A. and Williams, G.M., 2024. Lidar effective range. https://www.allegromicro.com/en/insights-and-innovations/technical-documents/p0177-lidar-effective-range
- Hurst, A.A., 2014. 3D Simulation of the Velodyne HDL-32E Lidar Integrated with an Autonomous Marine Vehicle. Daytona Beach, Florida: Embry-Riddle Aeronautical University, Master's thesis, 133p.
- Johnson, S.; Bethel, J.; Supunyachotsakul, C., and Peterson, S., 2016.
 Laser Mobile Mapping Standards and Applications in Transportation (Joint Transportation Research Program Publication No.

- FHWA/IN/JTRP-2016/01).West Lafayette, Indiana: Purdue University. 87p. doi:10.5703/1288284316164
- Kalvoda, P.; Nosek, J., and Kalvodova, P., 2021. Influence of control points configuration on the mobile laser scanning accuracy. IOP Conference Series: Earth and Environmental Science, 906, 012091. doi:10.1088/1755-1315/906/1/012091
- KellerLynn, K., 2010. Padre Island National Seashore: Geologic Resources Inventory Report. Fort Collins, Colorado: National Park Service, Natural Resource Report NPS/NRPC/GRD/NRR, 246p.
- Kelly, C.; Wilkinson, B.; Abd-Elrahman, A.; Cordero, O., and Lassiter, H.A., 2022. Accuracy assessment of low-cost Lidar scanners: An analysis of the Velodyne HDL-32E and Livox Mid-40's temporal stability. Remote Sensing, 14(17), 4220. doi:10.3390/rs14174220
- Kuçak, R.A.; Erol, S., and Erol, B., 2022. The strip adjustment of mobile LIDAR point clouds using iterative closest point (ICP) algorithm. Arabian Journal of Geosciences, 15, 1017. doi:10.1007/ s12517-022-10303-2
- Langridge, R.M.; Ries, W.F.; Farrier, T.; Barth, N.C.; Khajavi, N., and De Pascale, G.P., 2014. Developing sub 5-m LIDAR DEMs for forested sections of the Alpine and Hope faults, South Island, New Zealand: Implications for structural interpretations. *Journal of Structural Geology*, 64, 53–66. doi:10.1016/j.jsg.2013.11.007
- Le Mauff, B.; Juigner, M.; Ba, A.; Robin, M.; Launeau, P., and Fattal, P., 2018. Coastal monitoring solutions of the geomorphological response of beach-dune systems using multi-temporal LIDAR datasets (Vendée coast, France). *Geomorphology*, 304, 121–140. doi:10. 1016/j.geomorph.2017.12.037
- Ledoux, H. and Gold, C., 2005. An efficient natural neighbor interpolation algorithm for geoscientific modelling. *Developments in Spatial Data Handling*. Springer, Berlin, Heidelberg. doi:10.1007/3-540-26772-7_8
- Lewis, G., 2021. Using TerraMatch to apply strip adjustments to LIDAR data. https://geocue.com
- Li, Z.; Tan, J., and Liu, H., 2019. Rigorous Boresight Self-Calibration of Mobile and UAV LiDAR Scanning Systems by Strip Adjustment. Remote Sensing, 11(4), 442. doi:10.3390/rs11040442
- LiDARUSA, 2022. Successful field procedures. http://wiki.lidarusa.com/doku.php?id=successful_field_procedures
- Lim, S.; Thatcher, C.A.; Brock, J.C.; Kimbrow, D.R.; Danielson, J.J., and Reynolds, B.J., 2013. Accuracy assessment of a mobile terrestrial LIDAR survey at Padre Island National Seashore. *International Jour*nal of Remote Sensing, 34, 6355–6366. doi:10.1080/01431161.2013. 800658
- Lin, Y.C.; Liu, J.; Cheng, Y.T.; Hasheminasab, S.M.; Wells, T.; Bullock, D., and Habib, A., 2021. Processing strategy and comparative performance of different mobile LIDAR system grades for bridge monitoring: A case study. Sensors, 21(22), 7550. doi:10.3390/ s21227550
- Lin, Y.C.; Manish, R.; Bullock, D., and Habib, A., 2021. Comparative analysis of different mobile LIDAR mapping systems for ditch line characterization. *Remote Sensing*, 13(13), 2485. doi:10.3390/ rs13132485
- Liu, B.; Zhao, G.; Jiao, J.; Cai, G.; Li, C.; Yin, H.; Wang, Y.; Liu, M., and Hui, P., 2024. OmniColor: A Global Camera Pose Optimization Approach of LiDAR-360Camera Fusion for Colorizing Point Clouds, 2024 IEEE International Conference on Robotics and Automation (ICRA) (Yokohama, Japan), pp. 6396–6402. doi:10.1109/ICRA57147.2024.10610292
- Ma, L.; Li, Y.; Li, J.; Wang, C.; Wang, R., and Chapman, M.A., 2018.
 Mobile Laser Scanned Point-Clouds for Road Object Detection and Extraction: A Review. Remote Sensing, 10(10), 1531. doi:10.3390/rs10101531
- Mandlburger, G.; Kölle, M.; Pöppl, F., and Cramer, M., 2023. Evaluation of consumer-grade and survey-grade UAV-LIDAR. International Archives of the Photogrammetry, Remote Sensing and Spatial Information Sciences, XLVIII-1/W3, 99–106. doi:10.5194/isprs-archives-XLVIII-1-W3-2023-99-2023
- Montealegre, A.L.; Lamelas, M.T., and De la Riva, J., 2015. Interpolation Routines Assessment in ALS-Derived Digital Elevation Models for Forestry Applications. *Remote Sensing*, 7(7), 8631–8654. doi: 10.3390/rs70708631

- Nahon, A.; Molina, P.; Blázquez, M.; Simeon, J.; Capo, S., and Ferrero, C., 2019. Corridor mapping of sandy coastal foredunes with UAS photogrammetry and mobile laser scanning. *Remote Sensing*, 11(11), 1352. doi:10.3390/rs11111352
- Navmatix, 2024. GNSS mission planning. http://gnssmissionplanning.com/
- NGS (National Geodetic Survey), 2014. User guidelines for single base real-time GNSS positioning (v. 3.1). National Oceanic and Atmospheric Administration 66p. https://www.ngs.noaa.gov/PUBS_LIB/UserGuidelinesForSingleBaseRealTimeGNSSPositioningv.3. 1APR2014-1.pdf
- NGS (National Geodetic Survey), 2020. NOAA Technical Report NOS NGS 72 GEOID18. National Oceanic and Atmospheric Administration 94p. chrome-extension://efaidnbmnnnibpcajpcglclefindmkaj/https://geodesy.noaa.gov/library/pdfs/NOAA_TR_NOS_NGS_0072.pdf
- NGS (National Geodetic Survey), 2022. OPUS: Online Positioning User Service. https://geodesy.noaa.gov/OPUS/
- Nie, S.; Wang, C.; Dong, P.; Xi, X.; Luo, S., and Qin, H., 2017. A revised progressive TIN densification for filtering airborne LIDAR data. *Measurement*, 104, 70–77. doi:10.1016/j.measurement.2017. 03.007
- Niu, X.; Ban, Y.; Zhang, Q.; Zhang, T.; Zhang, H., and Liu, J., 2015.
 Quantitative Analysis to the Impacts of IMU Quality in GPS/INS
 Deep Integration. *Micromachines*, 6, 1082–1099. doi:10.3390/mi6081082
- NOAA (National Oceanic and Atmospheric Administration), 2024a. Coastal inundation dashboard. https://tidesandcurrents.noaa.gov/
- NOAA (National Oceanic and Atmospheric Administration), 2024b. Tides & currents. https://tidesandcurrents.noaa.gov/
- NOAA (National Oceanic and Atmospheric Administration), 2024c. Vertical datum transformation. https://tidesandcurrents.noaa.gov/
- NovAtel, 2013. Span-IGM user manual. https://hexagondownloads.blob.core.windows.net/public/Novatel/assets/Documents/Manuals/OM-20000141/OM-20000141.pdf
- NovAtel, 2024a. Common plots. https://docs.novatel.com/Waypoint/Content/Inertial_Explorer/Common_Plots_IE.htm
- NovAtel, 2024b. Processing direction. https://docs.novatel.com/Waypoint/ Content/GrafNav/Processing Direction.htm
- Olsen, M.J.; Roe, G.V.; Graig Glennie, Persi, F.; Reedy, M.; Hurwitz, D.; Williams, K.; Tuss, H.; Squellati, A., and Knodler, M., 2013. *Guidelines for the use of mobile LIDAR in transportation applications. NCHRP Report* 748, 66 pp, Transportation Research Board, Washington, D.C. https://ncalm.cive.uh.edu/sites/ncalm.cive.uh.edu/files/files/publications/reports/nchrp_rpt_748.pdf
- Open Source Geospatial Foundation, 2022. Geoid18 file. https://github.com/OSGeo/proj-datumgrid/blob/master/north-america/g2018u0.gtx
- Pendleton, E.A.; Thieler, R.; Williams, S.J.; and Beavers, R.L., 2004.
 Coastal Vulnerability Assessment of Padre Island National Seashore (PAIS) to Sea-Level Rise. U.S. Geological Survey Open-File Report 2004-1090, 25 pp, U.S. Geological Survey, Reston, VA. https://pubs.usgs.gov/of/2004/1090/ofr20041090.pdf
- Pennington, C.; Shaw, M.; Brooks, T.; Briganti, R.; Gomez-Pazo, A.; Ruffini, G.; Appleton, M., and Payo, A., 2024. Nine months of daily LiDAR, orthophotos and MetOcean data from the eroding soft cliff coast at Happisburgh, UK. Scientific Data, 11(846). doi:10.1038/ s41597-024-03499-3
- Pöppl, F.; Neuner, H.; Mandlburger, G., and Pfeifer, N., 2023. Integrated trajectory estimation for 3D kinematic mapping with GNSS, INS and imaging sensors: A framework and review. ISPRS Journal of Photogrammetry and Remote Sensing, 196, 287–305. doi:10.1016/j.isprsjprs.2022.12.022
- Puente, I.; González-Jorge, H.; Martínez-Sánchez, J., and Arias, P., 2013. Review of mobile mapping and surveying technologies. *Measure-ment*, 46, 2127–2145. doi:10.1016/j.measurement.2013.03.006
- Qin, N.; Tan, W.; Guan, H.; Wang, L.; Ma, L.; Tao, P.; Fatholahi, S.; Hu, X., and Li, J., 2023a. Towards intelligent ground filtering of large-scale topographic point clouds: a comprehensive survey. International Journal of Applied Earth Observation and Geoinformation, 125, 103566. doi:10.1016/j.jag.2023.103566

- Qin, N.; Tan, W.; Ma, L.; Zhang, D.; Guan, H., and Li, J., 2023b. Deep learning for filtering the ground from ALS point clouds: A dataset, evaluations and issues. *ISPRS Journal of Photogrammetry and Remote Sensing*, 202, 246–261. doi:10.1016/j.isprsjprs.2023.06.005
- Rakotosaona, M.; La Barbera, V.; Guerrero, P.; Mitra, N.J., and Ovsjanikov, M., 2020. PointCleanNet: Learning to denoise and remove outliers from dense point clouds. Computer Graphics Forum, 39, 185–203. doi:10.1111/cgf.13753
- Safran Sensing Technologies, 2019. Stim 300 inertial measurement unit. https://sensonor.azurewebsites.net/media/5z5lv25o/ts1524-r29-datasheet-stim300.pdf
- Schaer, P.; Skaloud, J.; Landtwing, S., and Legat, K., 2007. Accuracy Estimation for Laser Point Cloud Including Scanning Geometry. International Symposium on Mobile Mapping Technology, Padova, Italy. May 29–31, 2007. https://infoscience.epfl.ch/handle/20.500. 14299/17191
- Shaver, D.J.; Rubio, C.; Shelby Walker, J.; George, J.; Amos, A.F.; Reich, K.; Jones, C., and Shearer, T., 2016. Kemp's ridley sea turtle (*Lepidochelys kempii*) nesting on the Texas coast: Geographic, temporal, and demographic trends through 2014. Gulf of Mexico Science, 33(2), 158–178. doi:10.18785/goms.3302.04
- Sithole, G. and Vosselman, G., 2004. Experimental comparison of filter algorithms for bare-earth extraction from airborne laser scanning point clouds. *ISPRS Journal of Photogrammetry and Remote Sensing*, 59, 85–101. doi:10.1016/j.isprsjprs.2004.05.004
- Smeeckaert, J.; Mallet, C.; David, N.; Chehata, N., and Ferraz, A., 2013. Large-scale classification of water areas using airborne topographic lidar data. *Remote Sensing of Environment*, 138, 134–148. doi:10.1016/j.rse.2013.07.004
- Smith, T.; Rheinwalt, A., and Bookhagen, B., 2019. Determining the optimal grid resolution for topographic analysis on an airborne lidar dataset. *Earth Surface Dynamics*, 7(2), 475–489. doi:10.5194/esurf-7-475-2019
- Soininen, A., 2021. TerraMatch User Guide. Espoo, Finland: Terrasolid Ltd., 122p.
- Teledyne FLIR, 2023. Ladybug5+. https://www.flir.com/products/ladybug5plus/
- Trimble, 2024. Trimble GNSS planning online. https://www.gnssplanning.com/
- USACE (U.S. Army Corps of Engineers), 2024. Wave Information Study (WIS). https://wis.erdc.dren.mil/index.html
- Vaaja, M.; Hyyppä, J.; Kukko, A.; Kaartinen, H.; Hyyppä, H., and Alho, P., 2011. Mapping topography changes and elevation accuracies using a mobile laser scanner. *Remote Sensing*, 3(3), 587–600. doi:10.3390/rs3030587
- $\label{local-condition} \begin{tabular}{ll} Velodyne Lidar, Inc., 2018. HDL-$32E. $https://www.mapix.com/wp-content/uploads/2018/07/97-0038_Rev-M_-HDL-$32E_Datasheet_Web.pdf \end{tabular}$
- Wang, G.; Han, Y.; Chen, J.; Wang, S.; Zhang, Z.; Du, N., and Zheng, Y., 2018. A GNSS/INS integrated navigation algorithm based on Kalman filter. IFAC-PapersOnLine, 51(17), 232–237. doi:10.1016/j. ifacol.2018.08.151
- Weise, B.R. and White, W.A., 2007. Padre Island National Seashore: A Guide to the Geology, Natural Environments, and History of a Texas Barrier Island, Guidebook 17. Austin, Texas: University of Texas, Bureau of Economic Geology, 94p.
- Wheaton, J.M.; Brasington, J.; Darby, S.E., and Sear, D.A., 2010.
 Accounting for uncertainty in DEMs from repeat topographic surveys: Improved sediment budgets. *Earth Surface Processes and Landforms*, 35(2), 136–156. doi:10.1002/esp.1886
- White, S., 2007. Utilization of LIDAR and NOSS's Vertical Datum Transformation Tool (VDatum) for Shoreline Delineation. Oceans 2007, Vancouver, BC, Canada, 1–6. doi:10.1109/OCEANS.2007.4449147
- Xu, J.; Yao, C.; Ma, H.; Qian, C., and Wang, J., 2023. Automatic Point Cloud Colorization of Ground-Based LiDAR Data Using Video Imagery without Position and Orientation System. Remote Sensing. 15(10), 2658. doi:10.3390/rs15102658
- Yang, X.; Yan, G.; Yang, H., and Li, S., 2022. A GNSS aided initial alignment method for MEMS-IMU based on backtracking algorithm and backward filtering. arXiv [preprint]. http://arxiv.org/abs/ 2202.13700

Downloaded from https://prime-pdf-watermark.prime-prod.pubfactory.com/ at 2025-10-27 via free access

- Yen, K.S.; Ravani, B., and Lasky, T.A., 2011. LIDAR for data efficiency. Davis, California: Advanced Highway Maintenance and Construction Technology Research Center (Calif.), Washington (State) Department of Transportation, Report WA-RD 778.1. https://rosap.ntl.bts.gov/view/dot/23658
- Yu, J.; Lu, X.; Tian, M.; Chan, T.O., and Chen, C., 2021. Automatic extrinsic self-calibration of mobile LiDAR systems based on planar and spherical features. *Measurement Science and Technology*, 32, 065107. doi:10.1088/1361-6501/abecec
- Zhang, K.; Chen, S.C.; Whitman, D.; Shyu, M.L.; Yan, J., and Zhang, C., 2003. A progressive morphological filter for removing non-ground measurements from airborne LIDAR data. *IEEE Transactions on Geoscience and Remote Sensing*, 41(4), 872–882. doi:10.1109/TGRS.2003.810682
- Zhang, X.; Meng, X.; Li, C.; Shang, N.; Wang, J.; Xu, Y.; Wu, T., and Mugnier, C., 2021. Micro-topography mapping through terrestrial LIDAR in densely vegetated coastal environments. *ISPRS International Journal of Geo-Information*, 10(10), 665. doi:10.3390/ijgi10100665